Adaptive Identification of Nonlinear Friction and Load Torque for PMSM Drives via a Parallel-Observer-Based Network With Model Compensation

Chengbo Yang, *Student Member, IEEE*, Bao Song, Yuanlong Xie, *Member, IEEE*, Shiqi Zheng, *Senior Member, IEEE*, and Xiaoqi Tang

***Abstract*—Acquiring the accurate knowledge of nonlinear friction and load torque is of great interest for optimizing the control behavior of permanent-magnet synchronous motor drives. In this work, a friction-and-load adaptive identification scheme based on a parallel-observer-based network with model compensation (POBN-MC) is presented. The developed network possesses a parallel structure consisting of the designed two novel observers, which involve a gain-adaptation super-twisting load torque observer and a variable-learning-rate Adaline inertia observer. A nonempirical friction model is proposed to capture friction, forming the model compensation part that is exploited for correcting the torque input of the network. With a two-step mechanism derived from the POBN-MC, the proposed scheme attains the online adaptive identification of the friction and load torque in a manner that integrates both accuracy and simplicity. In the first step, an explicit mapping relationship between the nonlinear friction torque and the rotor speed is determined with the speed response triggered by the natural deceleration. The second step accomplishes the online observation with regard to friction-and-load information matching the real-time operating conditions. Sufficient theoretical analyses, as well as the validations of numerous simulations and experiments, are presented to support the suggested scheme.**

***Index Terms*—Adaline, adaptive identification, load toque, nonlinear friction toque, permanent-magnet synchronous motor (PMSM), super-twisting observer.**

Manuscript received 3 June 2022; revised 6 September 2022 and 4 December 2022; accepted 17 January 2023. Date of publication 24 January 2023; date of current version 10 March 2023. This work was supported in part by the National Key R&D Program of China under Grant 2020YFB1711300, in part by the Key R&D Project of Hubei under Grant 2022BAA061, in part by the National Natural Science Foundation of China under Grant 52105019, and in part by the Major Science and Technology Project of Guangdong under Grant 2020B090927001. Recommended for publication by Associate Editor N. Idris. *(Corresponding author: Bao Song.)*

Chengbo Yang, Bao Song, Yuanlong Xie, and Xiaoqi Tang are with the State Key Laboratory of Digital Manufacturing Equipment and Technology, School of Mechanical Science and Engineering, Huazhong University of Science and Technology, Wuhan 430074, China (e-mail: cb_yang@hust.edu.cn; songbao@hust.edu.cn; yuanlongxie@hust.edu.cn; xqtang@hust.edu.cn).

Shiqi Zheng is with the School of Automation, China University of Geosciences, Wuhan 430074, China, and also with the Hubei Key Laboratory of Advanced Control and Intelligent Automation for Complex Systems, Wuhan 430074, China (e-mail: zhengshiqi@cug.edu.cn).

Color versions of one or more figures in this article are available at https://doi.org/10.1109/TPEL.2023.3239609.

Digital Object Identifier 10.1109/TPEL.2023.3239609

I. Introduction

NOWADAYS, owing to the attractive virtues of high power density, superior torque-to-inertia ratio, and low acoustic noise, permanent-magnet synchronous motors (PMSMs) have drawn increasing attention in both industrial and domestic applications, such as robotic arms, machine tools, electric vehicles, and washing machines [1], [2], [3]. The knowledge of friction torque and load torque plays a crucial role in optimizing the speed control behavior of PMSM drives, especially for high-precision tracking and low-speed stability. A growing number of emerging speed control techniques, e.g., finite control set model predictive control [4], high-order sliding-mode control [5], and fuzzy sliding-mode control [6], are inseparable from precise friction and load information. Numerous techniques regarding the identification of friction-and-load torque have been put forward.

The existing approaches seeking to acquire the friction and load torque are able to fall into two categories, i.e., lumped-type and separate-type identification. In the lumped-type identification, the friction and load torque are modeled as a lumped parameter, and then this parameter is determined in real time by means of a certain observer, such as sliding-mode observer (SMO) [6], [7], [8], [9], disturbance observer (DOB) [10], [11], and extended state observer (ESO) [12], [13]. It should be pointed out, however, that the friction torque is speed-dependent and exhibits a highly nonlinear behavior, especially in the low-speed range. Moreover, when the motor operates at a bidirectional speed, abrupt friction torque changes will be induced. Hence, to cope with such a nonlinear and fast time-varying friction torque, a considerable observer gain has to be chosen in practical applications to guarantee the quality of the lumped identification. Unfortunately, the observer gain cannot be arbitrarily increased due to the inherent properties of the mechanical system or the observer. For instance, the gain of SMO is restricted owing to chattering suppression [14], while the gains of DOB and ESO are both limited by measurement noise and mechanical resonance [15]. Overall, identifying the friction-and-load torque in a lumped manner is bound to aggravate the burden of the observer, which may sacrifice the estimation accuracy and even result in identification failure and system instability.

As opposed to the lumped-type technique, the separate-type identification seems to be more potent and promising for obtaining the accurate knowledge of friction and load torque, as it distinguishes the friction torque and load torque. The separate-type identification can be sorted into two groups: simplified-friction-model-based technique (Type I) and accurate-friction-model-based technique (Type II). In Type I, the simplified friction model comprises the Coulomb and viscous friction torque or only considers the viscous friction torque. Several techniques have been reported to enable gaining the friction-and-load torque by using Type I, which mainly include multiparameter stepwise estimation [7], [16], [17] and multiparameter simultaneous estimation [15], [18], [19]. One important aspect, which deserves mentioning, is the fact that the simplified friction model is accurately able to describe the real friction behavior only under the premise that the drive system operates at high speeds [20], [21]. (The friction torque varies linearly with the rotor speed on this premise.) For non-high-speed operations (especially for low-speed operations), it is quite challenging to utilize Type I to gain high estimation accuracy on account of the nonlinearity of friction torque [22]. Overall, pursuing identification accuracy means that Type I has limited applicable working conditions. Fortunately, Type II is effectively capable of avoiding such an issue, as it establishes the accurate nonlinear friction model valid for the entire speed domain. In essence, Type II is able to be implemented based on a simple framework where the accurate friction model is incorporated into the torque signal channel of a load torque identification technique via feedforward compensation. Several schemes, such as [23], [24], [25], and [26], have made it possible to implement Type II. As far as the implementation framework is concerned, there are some advanced approaches available in the current literature. Therefore, it is necessary to present a brief review with regard to the existing exact friction models and load torque estimation methods to illustrate the technical issues of potential Type II.

In the extant literature, representative accurate nonlinear friction models primarily include the Stribeck model, LuGre model, Dahl model, generalized Maxwell-slip model, etc. Generally, extensive experimental tests are required to determine multiple unknown model parameters when exploiting these models to acquire the friction torque, which is directly responsible for causing their cumbersome and time-consuming implementation. Recently, Szczepanski et al. [27] contributed a promising solution for ameliorating the above-mentioned issue by developing a conventional artificial bee colony algorithm-based friction modeling technique, which can estimate the parameters of the Stribeck model accurately without the need for a tedious test procedure. Nevertheless, in practical applications, how to assure the search efficiency and solution quality of this technique needs to be further explored due to the potentially inappropriate parameter configurations and the inherent defects of the conventional artificial bee colony algorithm [28], [29]. Moreover, this approach has not accounted for the asymmetry of friction, which may lead to poor accuracy of the calculated friction torque in practice, as the friction torque is usually asymmetric over the whole speed domain [30]. In addition, and perhaps more importantly, the currently available nonlinear friction models, including the model involved in [27], are empirical models. When these models are unable to precisely characterize the actual plant model, the determined friction torque will deviate from the actual value even if the high-precision model parameter identification results are obtained. This is an inherent defect of the empirical friction models.

Previously reported load torque identification schemes can be mainly sorted into the following categories, i.e., the SMO [31], [32], full/reduced-order observer [33], extended Kalman filter (EKF) [34], model reference adaptive system (MRAS) [35], and algebraic estimation [36]. Among them, the SMO is receiving increasing attention on account of its inherently high robustness against noise, excellent insensitivity to parameter variations, and simple structure. Nevertheless, the first-order SMO (FO-SMO) suffers from chattering. The extended SMOs [32], [37], and the continuous functions (such as saturation function [31] and sigmoid function [38]) are able to be employed to diminish the chattering during the load torque identification without the need for a low-pass filter, which avoids the amplitude attenuation and the phase lag. Nonetheless, these approaches impose a compromise between the observation performance and chattering rejection, which sacrifices the inherent advantages of SMOs. The emergence of the second-order SMO (SO-SMO) makes it possible to maintain the advantages of the traditional SMO and, meanwhile, to lessen the chattering during the load torque identification. Moreover, the SO-SMO drives the load torque estimation error from exponential convergence to finite-time convergence, which contributes to enhancing observation performance and accuracy.

The current SO-SMOs identifying the load torque mainly include the super-twisting load torque SMO (ST-LT-SMO) [39], [40], terminal load torque SMO [16], and fast terminal load torque SMO [41]. Of note, compared with the other two observers, the ST-LT-SMO has fewer to-be-designed parameters, which makes it a more competitive candidate for observing the load torque. It should be pointed out that although these SO-SMOs are more attractive than the FO-SMO, an inherent challenge needs to be cause for concern. Namely, similar to the FO-SMO, in order to prevent the overestimation of gains, bound knowledge concerning the derivative of load torque is necessary for designing the SO-SMOs but is unknown in real-world applications. Furthermore, the previously reported SO-SMOs for identifying the load torque ignore the inertia mismatch, which will impair estimation accuracy under variable-speed operating conditions.

In conclusion, Type II is more promising and effective for the accurate identification of nonlinear friction and load torque. However, the currently available and potential techniques in this category suffer from the following major challenges.

1) The cumbersome and time-consuming implementation of the existing nonlinear friction models undermines the simplicity of gaining friction torque and is directly responsible for causing the fact that the Type II integrating both accuracy and simplicity remains lacking. In this regard, a novel friction modeling technique proposed by Szczepanski et al. [27] has made a significant contribution to counteract this defect, but neglecting the asymmetry of

friction poses a challenge to its accuracy for calculating the friction torque. Furthermore, it should be mentioned that the extant nonlinear friction models, including the model utilized in [27], are empirical models, which undoubtedly exacerbates the accuracy uncertainty of acquiring friction torque and results in the loss of generality.

2) The ST-LT-SMO is deemed to be a highly competitive candidate for estimating the load torque, but the previously reported ST-LT-SMOs carry several disadvantages (note that other SO-SMOs estimating the load torque also need to address the following issues).
   a) *A priori* knowledge regarding the boundary of the load torque derivative, which is difficult to obtain in advance, is required to prevent overestimating the gains.
   b) Inertia information is necessary for the load torque identification, and yet inertia mismatch is neglected.
   c) It is difficult to select suitable parameters matching the diverse PMSM-drive systems and their operating conditions to gain satisfactory identification performance.

In this article, an adaptive identification scheme using a parallel-observer-based network with model compensation (POBN-MC), which has not yet been reported in previous works, is proposed to tackle the aforementioned challenges. The dominating contributions are listed as follows.

1) A nonempirical equivalent friction model is put forward. It is devised using the analytical expression regarding the natural speed response induced by switching OFF the drive power. By defining the equivalent friction factor, the developed model exploits the natural speed response data to establish the friction model without the need for knowledge of the empirical components of friction (such as the viscous and Coulomb friction torque terms). Unlike the conventional nonlinear friction models relying on numerous experimental tests, the presented model is accurately able to determine the nonlinear friction torque with the aid of two natural speed response tests only. Moreover, different from the recently reported method in [27], our proposed friction model is directly capable of coping with the asymmetry of friction. More importantly, the developed model is a nonempirical model, which avoids additional accuracy uncertainty and improves the generality.
2) A gain-adaptation ST-LT-SMO is proposed, where all gains are able to change adaptively in accordance with the real-time sliding-mode surface. These ingenious time-varying gain designs force the observation error to converge to zero in finite time for any initial conditions. Compared with the existing ST-LT-SMOs (such as [39] and [40]), it has one and only one to-be-designed parameter, and meanwhile, it can automatically tune all gains to accommodate different PMSM-drive systems and their various operating conditions. Moreover, it no longer requires prior knowledge concerning the boundary regarding the derivative of the load torque, thereby preventing the overestimation of the gain values.
3) By resorting to the Adaline technique [42], a novel online inertia observer is developed to provide a calibrated inertia for the presented ST-LT-SMO. The convergence of the inertia observation error is reliably guaranteed with a variable learning rate. To the best of the authors' knowledge, this is the first time to utilize Adaline to directly attain the inertia identification. In comparison with the common online inertia estimation methods (see [43], [44], [45], [46], and their references), it not only has a more competitive computational burden but also covers several advantages at the same time, including unrestricted operating conditions, strict error convergence assurance, no neglects for the friction and load torque, and no matrix operations.
4) Based on the above-developed techniques, a POBN-MC is proposed. With the POBN-MC, an adaptive identification scheme that integrates both accuracy and simplicity is presented. It utilizes a two-step mechanism derived from the POBN-MC to attain the online and accurate observation of nonlinear friction and load torque. As a novel Type II, the suggested scheme addresses the aforementioned challenges faced by this class of techniques. Additionally, the whole scheme only requires adjusting two parameters, and their tuning guidelines are offered. The superior performance of our proposed scheme is confirmed with aiding from numerous simulations and experiments.

The rest of this article is organized as follows. In Section II, the PMSMs mathematical model is formulated. Section III elaborates on the proposed identification scheme by means of detailed derivations and analyses. Then, the simulation and experimental investigations concerning the suggested scheme are conducted in Section IV. Finally, Section V concludes this article.

II. PMSM Modeling

In the *dq*-axis reference frame, the dynamic model of a PMSM is generally able to be outlined as follows:

$$u_d = i_d R_m - i_q L_q P_n \omega_m + L_d \dot{i}_d \tag{1}$$

$$u_q = i_q R_m + P_n \omega_m L_d i_d + L_q \dot{i}_q + \psi_m P_n \omega_m \tag{2}$$

$$J\dot{\omega}_m = T_e - T_F(\omega_m) - T_L \tag{3}$$

$$T_e = 1.5 P_n i_q [\psi_f + (L_d - L_q) i_d] \tag{4}$$

where $i_d, i_q, u_d, u_q, P_n, R_m, L_d, L_q, \psi_m, J, \omega_m, T_e,$ and T_L stand for the *dq*-axis currents, *dq*-axis voltages, pole pair, stator resistance, *dq*-axis inductances, rotor flux linkage, total inertia, rotor speed, electromagnetic torque, and load torque, respectively. Additionally, $T_F(\omega_m)$ denotes the friction torque, which is a function of the rotor speed ω_m. The specific expression of $T_F(\omega_m)$ relies on the friction model utilized in the actual PMSM modeling. For instance, when applying the simplified friction model consisting of the Coulomb and viscous friction torque, its expression is given by

$$T_F(\omega_m) = B_m \omega_m + C_m \text{sign}(\omega_m) \tag{5}$$

where B_m and C_m represent the viscous and Coulomb friction coefficients, respectively. If employing the Stribeck model, then

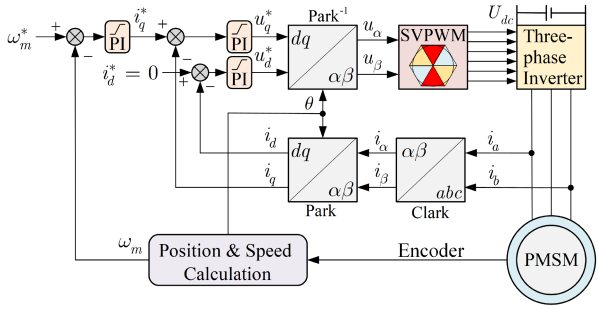

Fig. 1. Schematic diagram of the PMSM-drive system under the FOC.

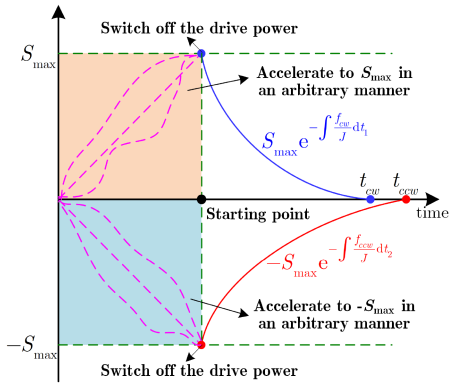

Fig. 2. Schematic representation of the natural speed responses under forward and reverse rotations.

$T_F(\omega_m)$ can be formulated as follows [21]:

$$T_F(\omega_m) = [F_a - C_m]\text{sign}(\omega_m)\text{e}^{-(\omega_m/\omega_a)} + B_m\omega_m + C_m\text{sign}(\omega_m) \tag{6}$$

where ω_a and F_a stand for the Stribeck speed and static friction torque, respectively.

As one of the mainstream control strategies, the field-oriented control (FOC) with $i_d^* = 0$ is commonly applied to the PMSM-driven system in real-world applications. Fig. 1 depicts the overall block diagram of this scheme. For a PMSM system, the accurate knowledge of the load torque T_L and the friction torque $T_F(\omega_m)$ is unknown but crucial for optimizing the control behavior. In this article, we focus on a friction-and-load adaptive identification scheme under the FOC framework to serve to gain accurate $T_F(\omega_m)$ and T_L, catering to the widespread demands mentioned in Section I.

III. Proposed Adaptive Identification Scheme

A. Nonempirical Equivalent Friction Model

For the sake of achieving the friction feedforward under the framework of Type II, the friction model is supposed to be determined first. In this article, a nonempirical equivalent friction model is proposed for the first time. The detailed description/design is given in the following text. In practice, the friction model is established during the system commissioning so as to ensure that the friction torque can be properly compensated during the period in which the drive system is put into mission operation. It should be pointed out that during the system commissioning, there is generally no external disturbance (i.e., the load torque can be deemed as zero) and the inertia is constant [15], [22] (notice that during the mission, the load torque is usually present and variable, and the inertia may also vary). As a consequence, during friction modeling, (3) can be rewritten as follows:

$$\dot{\omega}_m = \frac{T_e - T_F(\omega_m)}{J}. \tag{7}$$

When the PMSM-drive system is accelerated to the allowable maximum speed in an arbitrary manner, the system will naturally decelerate to zero if the drive power is switched OFF. During this period, owing to the absence of the electromagnetic torque T_e, (7) becomes

$$\dot{\omega}_{md} = -\frac{T_F(\omega_{md})}{J} \tag{8}$$

where ω_{md} stands for the speed response due to the natural deceleration.

Here, we introduce two equivalent friction factors and utilize the products with regard to the two and the rotor speed to describe the asymmetry of friction over the whole speed domain, i.e.

$$T_F(\omega_m) = \begin{cases} f_{cw}\omega_m, & \text{if } \omega_m > 0 \\ 0, & \text{if } \omega_m = 0 \\ f_{ccw}\omega_m, & \text{if } \omega_m < 0 \end{cases} \tag{9}$$

where f_{cw} and f_{ccw} are the equivalent friction factors under the forward and reverse rotations of the drive motor, respectively. Using (9), (8) is able to be rewritten as follows:

$$\dot{\omega}_{md} = \begin{cases} -\frac{f_{cw}\omega_{md}}{J}, & \text{if } \omega_{md} > 0 \\ 0, & \text{if } \omega_{md} = 0 \\ -\frac{f_{ccw}\omega_{md}}{J}, & \text{if } \omega_{md} < 0. \end{cases} \tag{10}$$

Defining the allowable maximum speed as $S_{\max}$, one can derive the analytic expression of (10) as follows:

$$\omega_{md} = \begin{cases} S_{\max}\text{e}^{-\int \frac{f_{cw}}{J} dt_1}, & \text{if } \omega_{md} > 0 \\ 0, & \text{if } \omega_{md} = 0 \\ -S_{\max}\text{e}^{-\int \frac{f_{ccw}}{J} dt_2}, & \text{if } \omega_{md} < 0 \end{cases} \tag{11}$$

where t_1 and t_2 denote the natural deceleration time variables of the motor's two rotation directions, respectively. Note that if the moment that the motor starts to decelerate naturally is treated as the zero time point, then $t_1 \in [0, t_{cw}]$ and $t_2 \in [0, t_{ccw}]$, where t_{cw} and t_{ccw} represent the time it takes for the motor to naturally decelerate from $S_{\max}$ and zero and from $-S_{\max}$ to zero, respectively. Fig. 2 presents the schematic representation of the natural speed responses under forward and reverse rotations of the drive motor.

The mathematical relationship between the natural speed response and the deceleration time is precisely described by (11). Then, in order to acquire the equivalent friction factors f_{cw} and f_{ccw}, this article applies the simple and easy-to-implement curve

fitting. To be specific, (11) is fitted as follows:

$$\omega_{md}=\begin{cases}S_{\max}\mathrm{e}^{-\int\frac{\hat{f}_{cw}}{J}dt_1}=S_{\max}\mathrm{e}^{p(t_1)}, & \text{if } \omega_{md}>0\\ 0, & \text{if } \omega_{md}=0\\ S_{\max}\mathrm{e}^{-\int\frac{\hat{f}_{ccw}}{J}dt_2}=S_{\max}\mathrm{e}^{q(t_2)}, & \text{if } \omega_{md}<0\end{cases} \tag{12}$$

where $\hat{f}_{cw}$ and $\hat{f}_{ccw}$ are the estimated values of f_{cw} and f_{ccw}, respectively; $p(t_1)=p_rt_1^r+p_{r-1}t_1^{r-1}+\cdots+p_1t_1+p_0$ and $q(t_2)=q_ht_2^h+q_{h-1}t_2^{h-1}+\cdots+q_1t_2+q_0$, which represent the fitted polynomials. Note that p_x and q_y $(x=r,r-1,\ldots,0;\ y=h,h-1,\ldots,0)$ stand for the fitting coefficients, and r and h are the orders of the polynomials $p(t_1)$ and $q(t_2)$, respectively. It should be pointed out that, in practical applications, the values of r and h may be different due to the asymmetry of friction. In order to select their appropriate values, an automatic-order-determination technique will be developed later (see Section III-D).

Based on (12), one can obtain

$$\begin{cases}\frac{\hat{f}_{cw}}{J}=\dot{p}(t_1)=rp_rt_1^{r-1}+(r-1)p_{r-1}t_1^{r-2}+\cdots+p_1\\ \frac{\hat{f}_{ccw}}{J}=\dot{q}(t_2)=hq_ht_2^{h-1}+(h-1)q_{h-1}t_2^{h-2}+\cdots+q_1\end{cases}. \tag{13}$$

The above equation indicates that the two equivalent friction factors can be determined using the inertia information and the fitting results corresponding to the natural speed response data of the motor's two directions. Once the equivalent friction factors are gained, the friction torque matching each speed over the whole speed domain is able to be calculated/identified online, i.e.,

$$\hat{T}_F(\omega_m)=\begin{cases}\hat{f}_{cw}\omega_m, & \text{if } \omega_m>0\\ 0, & \text{if } \omega_m=0\\ \hat{f}_{ccw}\omega_m, & \text{if } \omega_m<0\end{cases} \tag{14}$$

where $\hat{T}_F(\omega_m)$ stands for the identified/calculated value of $T_F(\omega_m)$.

To summarize, the developed friction model is composed of (12), (13), and (14). The detailed implementation process with respect to this model will be introduced later. In addition, it can be noticed from the design process that the proposed model is a nonempirical model based on the natural speed response data, which is capable of obtaining the friction torque matching each speed without the need for detailed knowledge of the empirical components of friction.

Remark 1: According to (13), one can know that the determination of the two equivalent friction factors requires knowledge of inertia. In real-world applications, the total inertia J is usually partially known. During friction modeling, suppose that J_0 stands for the known part of the total inertia (e.g., the motor inertia) and ΔJ represents the unknown part of total inertia (e.g., the load inertia). Then, we have $J=J_0+\Delta J$. Thereupon, (13) can be rewritten as follows:

$$\begin{cases}\hat{f}_{cw}=J_0\dot{p}(t_1)+\Delta J\dot{p}(t_1)\\ \hat{f}_{ccw}=J_0\dot{q}(t_2)+\Delta J\dot{q}(t_2)\end{cases} \tag{15}$$

which reveals that the estimated values of the two equivalent factors vary linearly with the unknown part of the total inertia. This means that the accurate inertia information has to be provided in order to guarantee friction modeling accuracy. In this article, a parallel-observer-based network will be developed later, which aims to avoid the inertia mismatch during load torque identification. Here, it should be pointed out that it actually has an additional role, i.e., it is capable of offering the accurate inertia correction during friction modeling. More details will be described in Section III-D.

B. Gain-Adaptation ST-LT-SMO

When the friction torque is counteracted, the mechanical model (3) is able to be simplified to

$$\dot{\omega}_m=j(T_e^c-T_L) \tag{16}$$

where $j=1/J$, and T_e^c represents the electromagnetic torque removing friction, i.e., $T_e^c=T_e-T_F(\omega_m)$.

Regarding both ω_m and T_L as state variables, (16) can be extended to

$$\begin{cases}\dot{\omega}_m=j(T_e^c-T_L)\\ \dot{T}_L=d\end{cases} \tag{17}$$

where d stands for the time derivative of the load torque T_L.

According to (17) and by means of the standard super-twisting algorithm [47], a conventional ST-LT-SMO can be designed as follows:

$$\begin{cases}\dot{\hat{\omega}}_m=j[T_e^c-\hat{T}_L-\delta_1|e_{\omega m}|^{1/2}\mathrm{sign}(e_{\omega m})]\\ \dot{\hat{T}}_L=\delta_2\mathrm{sign}(e_{\omega m})\end{cases} \tag{18}$$

where $\hat{\omega}_m$ and $\hat{T}_L$ are the identified values of $\hat{\omega}_m$ and $\hat{T}_L$, respectively; $e_{\omega m}=\hat{\omega}_m-\omega_m$; δ_1 and δ_2 are the gains of the standard ST-LT-SMO.

As described in [47], introducing the additional linear term is able to improve the identification behavior of the standard super-twisting algorithm. Consequently, an enhanced ST-LT-SMO can be described as follows:

$$\begin{cases}\dot{\hat{\omega}}_m=j[T_e^c-\hat{T}_L-k_1|e_{\omega m}|^{1/2}\mathrm{sign}(e_{\omega m})-k_2e_{\omega m}]\\ \dot{\hat{T}}_L=k_3\mathrm{sign}(e_{\omega m})+k_4e_{\omega m}\end{cases} \tag{19}$$

where k_1,k_2,k_3, and k_4 are the observer gains. It should be noted that the gain designs for both conventional and enhanced ST-LT-SMOs require knowledge regarding the boundary of the load torque derivative. Nevertheless, the boundary is not readily known. Furthermore, it is difficult to find appropriate gains to match the different drive systems and operating conditions. In this article, based on the observer (19), we propose a gain-adaptation ST-LT-SMO, which is given by

$$\begin{cases}\dot{\hat{\omega}}_m=j[T_e^c-\hat{T}_L-\frac{1}{4}k(e_{\omega m})|e_{\omega m}|^{1/2}\mathrm{sign}(e_{\omega m})\\ \quad -\frac{1}{4}k(e_{\omega m})e_{\omega m}]\\ \dot{\hat{T}}_L=\frac{1}{2}k^2(e_{\omega m})\mathrm{sign}(e_{\omega m})+k^2(e_{\omega m})e_{\omega m}\end{cases} \tag{20}$$

where $k(e_{\omega m})$ is the designed time-variable gain function, which satisfies

$$\begin{cases} k(e_{\omega m}) = |a(e_{\omega m})| \\ \dot{a}(e_{\omega m}) = \frac{\eta}{\mathrm{e}^{-|e_{\omega m}|}} \mathrm{sign}(e_{\omega m}) \end{cases} \tag{21}$$

where η stands for the integral scale factor ($\eta > 0$). Note that in (21), the initial value of $k(e_{\omega m})$ is set as a tiny arbitrary positive number (e.g., 0.001) so that $k(e_{\omega m}) > 0$ always holds. From (20), it can be noticed that the gains k_1, k_2, k_3, and k_4 in the observer (19) are devised as $k_1 = 0.25k(e_{\omega m})$, $q(t_2) = 0.25k(e_{\omega m})$, $k_3 = 0.5k^2(e_{\omega m})$, and $k_4 = k^2(e_{\omega m})$, respectively.

By subtracting (17) from (20), the error equation of the gain-adaptation ST-LT-SMO (20) can be obtained as follows:

$$\begin{cases} \dot{e}_{\omega m} = j\big[- e_{TL} - \frac{1}{4}k(e_{\omega m})|e_{\omega m}|^{1/2}\mathrm{sign}(e_{\omega m}) \\ \qquad -\frac{1}{4}k(e_{\omega m})e_{\omega m}\big] \\ \dot{e}_{TL} = \frac{1}{2}k^2(e_{\omega m})\mathrm{sign}(e_{\omega m}) + k^2(e_{\omega m})e_{\omega m} - d \end{cases} \tag{22}$$

where $e_{TL} = \hat{T}_L - T_L$. It should be pointed out that in practice, the time derivative of T_L, i.e., d, is clearly bounded. Here, d is defined by $|d| \le \gamma_1 + \gamma_2|e_{\omega m}|$ [47], where γ_1 and γ_2 are the positive constants. Let $e_1 = e_{\omega m}$ and $e_2 = -e_{TL}$, we can rewrite (22) as follows:

$$\begin{cases} \dot{e}_1 = j\left[e_2 - \frac{1}{4}k(e_1)|e_1|^{1/2}\mathrm{sign}(e_1) - \frac{1}{4}k(e_1)e_1\right] \\ \dot{e}_2 = -\frac{1}{2}k^2(e_1)\mathrm{sign}(e_1) - k^2(e_1)e_1 + d. \end{cases} \tag{23}$$

Then, we can derive the following result.

Theorem 1: For any initial conditions $e_1(0)$ and $e_2(0)$, the errors e_1 and e_2 will converge to zero in finite time if the designed time-variable gain function $k(e_1)$ satisfies

$$k(e_1) > \mathrm{MAX}\left(\sqrt{\frac{32}{17}}\gamma_1, \sqrt{\frac{1}{2}}\gamma_2, \sqrt{\Theta_1}, \sqrt{\Theta_2}\right) \tag{24}$$

where

$$\begin{cases} \Theta_1 = -b_1/3a_1 + 2\sqrt{-\mu_1}\cos(\arccos(\rho_1/(-\mu_1)^{3/2})/3) \\ \Theta_2 = -b_2/3a_2 + 2\sqrt{-\mu_2}\cos(\arccos(\rho_2/(-\mu_2)^{3/2})/3) \end{cases} \tag{25}$$

with the following notations and definitions:

$$\begin{cases} a_1 = 439 \\ b_1 = -3264\gamma_1 - 512\gamma_2 \\ c_1 = -37888\gamma_1^2 + 3072\gamma_1\gamma_2 \\ d_1 = 32768\gamma_1^2\gamma_2 \\ \rho_1 = -\frac{b_1^3}{27a_1^3} - \frac{d_1}{2a_1} + \frac{b_1c_1}{6a_1^2} \\ \mu_1 = \frac{c_1}{3a_1} - \frac{b_1^2}{9a_1^2} \end{cases} \text{and} \begin{cases} a_2 = 5 \\ b_2 = -8\gamma_1 - 15\gamma_2 \\ c_2 = -80\gamma_2^2 + 24\gamma_1\gamma_2 \\ d_2 = 128\gamma_1\gamma_2^2 \\ \rho_2 = -\frac{b_2^3}{27a_2^3} - \frac{d_2}{2a_2} + \frac{b_2c_2}{6a_2^2} \\ \mu_2 = \frac{c_2}{3a_2} - \frac{b_2^2}{9a_2^2}. \end{cases}$$

Proof: Let us consider a new Lyapunov function, which is given by

$$V = \xi^T P\xi/k^4(e_1) \tag{26}$$

where

$$\xi = \begin{bmatrix} |e_1|^{1/2}\mathrm{sign}(e_1) \\ e_1 \\ e_2 \end{bmatrix}, \text{ and } P$$

$$= \frac{1}{2}\begin{bmatrix} \frac{33}{16}k^2(e_1) & \frac{1}{16}k^2(e_1) & -\frac{1}{4}k(e_1) \\ \frac{1}{16}k^2(e_1) & \frac{33}{16}k^2(e_1) & -\frac{1}{4}k(e_1) \\ -\frac{1}{4}k(e_1) & -\frac{1}{4}k(e_1) & 2 \end{bmatrix}.$$

Therefore, we can derive the following:

$$\dot{V} = \underbrace{\xi^T\dot{Q}\xi}_{\dot{V}_a} + \underbrace{2\dot{\xi}^TQ\xi}_{\dot{V}_b} \tag{27}$$

where $Q = P/k^4(e_1)$. It is observed that (27) can be separated into two components for further analysis, as described in the following text.

Component 1: The first component $\dot{V}_a$ can be expressed in detail as follows:

$$\dot{V}_a = \frac{1}{2}\xi^T\left\{\dot{k}(e_1)\underbrace{\begin{bmatrix} -\frac{33}{8}k^{-3}(e_1) & -\frac{1}{8}k^{-3}(e_1) & \frac{3}{4}k^{-4}(e_1) \\ -\frac{1}{8}k^{-3}(e_1) & -\frac{33}{8}k^{-3}(e_1) & \frac{3}{4}k^{-4}(e_1) \\ \frac{3}{4}k^{-4}(e_1) & \frac{3}{4}k^{-4}(e_1) & -8k^{-5}(e_1) \end{bmatrix}}_{M}\right\}\xi$$

$$= \frac{1}{2}\dot{k}(e_1)\xi^TM\xi. \tag{28}$$

According to (21), we can derive that

$$\dot{k}(e_1) = \dot{a}(e_1)\mathrm{sign}[a(e_1)] \le \dot{a}(e_1) \le \frac{\eta}{\mathrm{e}^{-|e_1|}} \tag{29}$$

is satisfied. As a result, (28) can be rewritten as

$$\dot{V}_a = \frac{1}{2}\dot{k}(e_1)\xi^TM\xi \le \frac{1}{2}\dot{a}(e_1)\xi^TM\xi \le \frac{\eta}{2\mathrm{e}^{-|e_1|}}\xi^TM\xi. \tag{30}$$

Notice that the matrix M is negative definite due to the fact that $k(e_{\omega m}) > 0$ holds. Therefore, we have

$$\dot{V}_a \le \frac{\eta}{2e^{-|e_1|}}\xi^TM\xi < 0. \tag{31}$$

Component 2: For the second component $\dot{V}_b$, we can obtain

$$\dot{V}_b = 2\dot{\xi}^TQ\xi = -|e_1|^{-1/2}\xi^T$$

$$\underbrace{\left\{\frac{1}{8}k^{-3}(e_1)\begin{bmatrix} \frac{17}{16}k^2(e_1) & 0 & -\frac{1}{4}k(e_1) \\ 0 & \frac{37}{16}k^2(e_1) & -\frac{3}{4}k(e_1) \\ -\frac{1}{4}k(e_1) & -\frac{3}{4}k(e_1) & 1 \end{bmatrix}\right\}}_{\mathrm{X}_1}\xi$$

$$-\xi^T\underbrace{\left\{\frac{1}{4}k^{-3}(e_1)\begin{bmatrix} \frac{5}{8}k^2(e_1) & 0 & 0 \\ 0 & \frac{17}{16}k^2(e_1) & -\frac{1}{4}k(e_1) \\ 0 & -\frac{1}{4}k(e_1) & 1 \end{bmatrix}\right\}}_{\mathrm{X}_2}\xi$$

$$+\underbrace{\begin{bmatrix} -\frac{1}{4}k^{-3}(e_1)d & -\frac{1}{4}k^{-3}(e_1)d & 2k^{-4}(e_1)d \end{bmatrix}}_{\chi_1^T}\xi$$

$$= -|e_1|^{-1/2}\xi^T\mathrm{X}_1\xi - \xi^T\mathrm{X}_2\xi + \chi_1^T\xi. \tag{32}$$

Defining $\phi^T = [|e_1|^{1/2} \quad |e_1| \quad |e_2|]$ and using the relationship $|d| \le \gamma_1 + \gamma_2|e_1|$, we have

$$\begin{cases} -|e_1|^{-1/2}\xi^T \mathrm{X}_1 \xi - \xi^T \mathrm{X}_2 \xi \le -|e_1|^{-1/2}\phi^T \mathrm{X}_1 \phi - \phi^T \mathrm{X}_2 \phi \\ \chi_1^T \xi \le |e_1|^{-1/2}\phi^T \Delta_1 \phi + \phi^T \Delta_2 \phi \end{cases} \tag{33}$$

where

$$\Delta_1 = \begin{bmatrix} \frac{1}{4}k^{-3}(e)\gamma_1 & 0 & k^{-4}(e)\gamma_1 \\ 0 & \frac{1}{4}k^{-3}(e)\gamma_2 & 0 \\ k^{-4}(e)\gamma_1 & 0 & 0 \end{bmatrix}$$

$$\Delta_2 = \begin{bmatrix} \frac{1}{4}k^{-3}(e)\gamma_1 & 0 & 0 \\ 0 & \frac{1}{4}k^{-3}(e)\gamma_2 & k^{-4}(e)\gamma_2 \\ 0 & k^{-4}(e)\gamma_2 & 0 \end{bmatrix}.$$

Combining (32) and (33) yields

$$\begin{aligned} \dot{V}_b &= -|e_1|^{-1/2}\xi^T \mathrm{X}_1 \xi - \xi^T \mathrm{X}_2 \xi + \chi_1^T \xi \\ &\le -|e_1|^{-1/2}\phi^T \{\mathrm{X}_1 - \Delta_1\}\phi - \phi^T \{\mathrm{X}_2 - \Delta_2\}\phi. \end{aligned} \tag{34}$$

Of note, $\dot{V}_b < 0$ if the matrices $\mathrm{X}_1 - \Delta_1$ and $\mathrm{X}_2 - \Delta_2$ are the positive definite. Obviously, this case is true provided that the time-variable gain function $k(e_{\omega m})$ fulfills (24).

Consider the following facts:

$$\lambda_{\min}\{Q\}\|\xi\|_2^2 \le V = \xi^T Q \xi \le \lambda_{\max}\{Q\}\|\xi\|_2^2 \tag{35}$$

and

$$\begin{aligned} \lambda_{\min}\{\mathrm{X}_1 - \Delta_1\}\|\phi\|_2^2 &\le \phi^T \{\mathrm{X}_1 - \Delta_1\}\phi \\ &\le \lambda_{\max}\{\mathrm{X}_1 - \Delta_1\}\|\phi\|_2^2 \end{aligned} \tag{36}$$

where $\lambda_{\min}\{\cdot\}$ and $\lambda_{\max}\{\cdot\}$ denote the minimum and maximum eigenvalues of a matrix, respectively; $\|\cdot\|_2^2$ represents the Euclidean norm.

Then, using (35), (36), and the fact that

$$|e_1|^{1/2} \le \|\xi\|_2 \le \frac{V^{1/2}}{\lambda_{\min}^{1/2}\{Q\}}, \tag{37}$$

it follows that (34) can be rewritten as follows:

$$\begin{aligned} \dot{V}_b \le & -|e_1|^{-1/2}\phi^T \{\mathrm{X}_1 - \Delta_1\}\phi - \phi^T \{\mathrm{X}_2 - \Delta_2\}\phi \\ \le & -|e_1|^{-1/2}\phi^T \{\mathrm{X}_1 - \Delta_1\}\phi \\ \le & -|e_1|^{-1/2}\lambda_{\min}\{\mathrm{X}_1 - \Delta_1\}\|\phi\|_2^2 \\ = & -|e_1|^{-1/2}\lambda_{\min}\{\mathrm{X}_1 - \Delta_1\}\|\xi\|_2^2 \\ \le & -\frac{\lambda_{\min}^{1/2}\{Q\}\lambda_{\min}\{\mathrm{X}_1 - \Delta_1\}}{V^{1/2}\lambda_{\max}\{Q\}}V \\ = & -\frac{\lambda_{\min}^{1/2}\{Q\}\lambda_{\min}\{\mathrm{X}_1 - \Delta_1\}}{\lambda_{\max}\{Q\}}V^{1/2} \end{aligned} \tag{38}$$

which results in

$$\dot{V} = \underbrace{\xi^T \dot{Q} \xi}_{\dot{V}_a} + \underbrace{2\dot{\xi}^T Q \xi}_{\dot{V}_b}$$

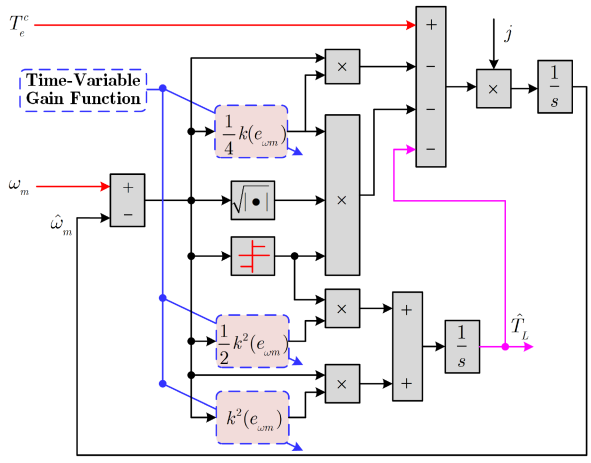

Fig. 3. Schematic block diagram of the proposed ST-LT-SMO.

$$< \dot{V}_b \le -\frac{\lambda_{\min}^{1/2}\{Q\}\lambda_{\min}\{\mathrm{X}_1 - \Delta_1\}}{\lambda_{\max}\{Q\}}V^{1/2}. \tag{39}$$

Considering (39) and the comparison lemma, it is easily concluded that e_1 and e_2 can converge to zero in finite time. This ends the proof. Fig. 3 depicts the principle block diagram of the proposed gain-adaptation ST-LT-SMO.

Remark 2: It is noteworthy that for finite-time convergence, the time-varying gain function $k(e_1)$ must satisfy the condition (24). This implies that $k(e_1)$ shall increase in accordance with (21) until (24) holds. After that, the finite-time convergence is guaranteed according to (39).

C. Adaline-Based Inertia Online Observer

For load torque identification, inertia knowledge is necessary. In order to prevent our proposed gain-adaptation ST-LT-SMO (20) from the inertia mismatch, a novel online inertia observer is developed using the Adaline technique. The detailed design with regard to this inertia observer is described as follows.

The discrete-time version for (16) is able to be expressed as follows:

$$\omega_m(n+1) = \omega_m(n) + T_c j(n+1)[T_e^c(n+1) - T_L(n+1)] \tag{40}$$

where n stands for the discrete sampling moment and T_c is the speed-loop sampling period.

According to (40), an Adaline-based inertia observer with a variable learning rate is proposed, which is given by

$$\begin{cases} \underbrace{\hat{\omega}_m(n+1)}_{\text{Adaline's output}} = \underbrace{1}_{\text{Wight 1}} \cdot \underbrace{\omega_m(n)}_{\text{Input 1}} \\ \quad + \underbrace{\hat{j}(n+1)}_{\text{Wight 2}} \cdot \underbrace{T_c[T_e^c(n+1) - T_L(n+1)]}_{\text{Input 2}} \\ \underbrace{\hat{j}(n+1) = \hat{j}(n) + \beta(n)e_i(n)I(n)}_{\text{The training formula of the Weight 2}} \\ \beta(n) = \frac{\beta_0}{[T_c T_{\max} - T_c T_L(n)]^2} \end{cases} \tag{41}$$

where $\hat{j}$ is the estimated value of j and satisfies $j = 1/\hat{J}$ ($\hat{J}$ is the identified value of J); $e_i(n) = \omega_m(n) - \hat{\omega}_m(n)$;

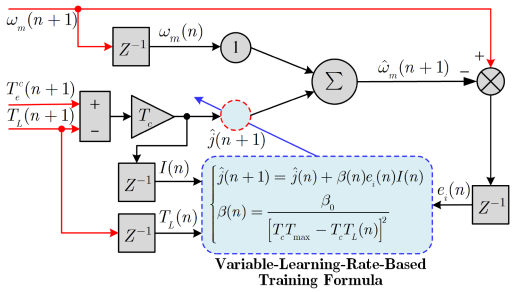

Fig. 4. Schematic block diagram of the developed Adaline-based inertia observer.

$I(n) = T_c T_e^c(n) - T_c T_L(n)$; β stands for the designed time-varying learning rate; β_0 satisfies $0 < \beta_0 < 2$; $T_{\max}$ represents the maximum torque of the PMSM-drive system, which is usually three times the rated torque T_N, i.e., $T_{\max} = 3T_N$.

Theorem 2: If an online inertia observer is devised as (41), then $\hat{j}$ will converge to its actual value j asymptotically.

Proof: Defining $e_j(n) = j - \hat{j}(n)$, we can derive

$$\begin{aligned} e_i(n) &= \omega_m(n) - \hat{\omega}_m(n) \\ &= \omega_m(n) - \left\{\omega_m(n-1) + T_c\hat{j}(n)\left[T_e^c(n) - T_L(n)\right]\right\} \\ &= T_c j(n)\left[T_e^c(n) - T_L(n)\right] - T_c\hat{j}(n)\left[T_e^c(n) - T_L(n)\right] \\ &= I(n)e_j(n). \end{aligned} \tag{42}$$

Then, choosing a Lyapunov function as $V_j(n) = e_j^2(n)$, we have

$$\begin{aligned} \Delta V_j(n) &= V_j(n+1) - V_j(n) \\ &= e_j^2(n+1) - e_j^2(n) \\ &= \left[j - \hat{j}(n+1)\right]^2 - e_j^2(n) \\ &= \left[j - \hat{j}(n) - \beta(n)e_i(n)I(n)\right]^2 - e_j^2(n) \\ &= \left[e_j(n) - \beta(n)e_i(n)I(n)\right]^2 - e_j^2(n) \\ &= -2\beta(n)e_j^2(n)I^2(n) + \beta^2(n)e_j^4(n)I^4(n). \end{aligned} \tag{43}$$

Substituting $\beta(n) = \beta_0/[T_c T_{\max} - T_c T_L(n)]^2$ into (43) yields that $\Delta V_j(n) = e_j^2(n)I^2(n)\beta(n)[-2 + \beta(n)I^2(n)] < 0$ for $e_j(n) \neq 0$. Hence, one can draw the conclusion that the inertia estimation error $e_j(n)$ converges to zero asymptotically. This finishes the proof. From the proof process, it can be easily seen that, in essence, the ingenious variable-learning-rate design is to guarantee the reliable convergence of the inertia observation error. Fig. 4 displays the principle block diagram of the developed Adaline-based inertia observer.

Remark 3: A qualitative comparison concerning the presented inertia observer and the common online inertia-identification methods is given in Fig. 5. From there, one can readily find that only our proposed Adaline-based inertia observer possesses all the mentioned virtues. In Section IV, the actual identification performance comparison and the quantitative comparison regarding the execution time in the STM32 microprocessor will be conducted to further highlight the superiority of the developed inertia observer.

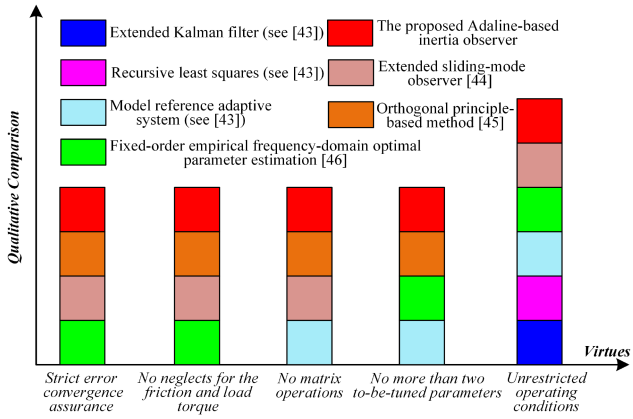

Fig. 5. Qualitative comparison concerning the presented inertia observer and the common online inertia-identification methods.

Remark 4: In the proofs of Theorems 1 and 2, it is noticed that the identification errors e_j and e_{TL} can converge to zero over time without relying on the initial conditions $\hat{J}(0)$ and $\hat{T}_L(0)$. This implies that $\hat{J}(0)$ and $\hat{T}_L(0)$ can be initialized with arbitrary values.

D. Adaptive Friction-and-Load Identification Scheme Using a Two-Step Mechanism

Figs. 3 and 4 have clearly demonstrated the principle of the proposed ST-LT-SMO and the developed inertia observer. Based on these two observers, this article presents a parallel-observer-based network, as shown in Fig. 6(a). From there, it can be observed that the ST-LT-SMO (20) and the inertia observer (41) operate in parallel and offer real-time updates to each other. The observed value of the proposed ST-LT-SMO is fed into the developed inertia observer as an input variable, and meanwhile, the latter provides online inertia correction for the former. Fig. 6(b) gives the detailed parameter estimation process of this network. By incorporating the designed nonempirical equivalent friction model into the proposed parallel-observer-based network, this article presents a POBN-MC, as displayed in Fig. 7. From there, it can be noticed that the nonempirical equivalent friction model-based model compensation part is concatenated with the parallel-observer-based network in a feedforward manner (it aims to counteract the friction torque in the torque signal channel).

Then, an adaptive identification scheme using the POBN-MC is presented to acquire the nonlinear friction torque and load torque accurately. The suggested scheme utilizes a two-step identification mechanism derived from our developed POBN-MC to serve the estimation purpose. Fig. 8 exhibits the detailed principle of the proposed friction-and-load identification scheme (a detailed description of Fig. 8 will be given later). Notice that the first step is employed in the system commissioning process (at this time, the load torque can be deemed as zero and the inertia is constant, as mentioned in Section III-A), while the second step is applied during the mission (at this time, the load

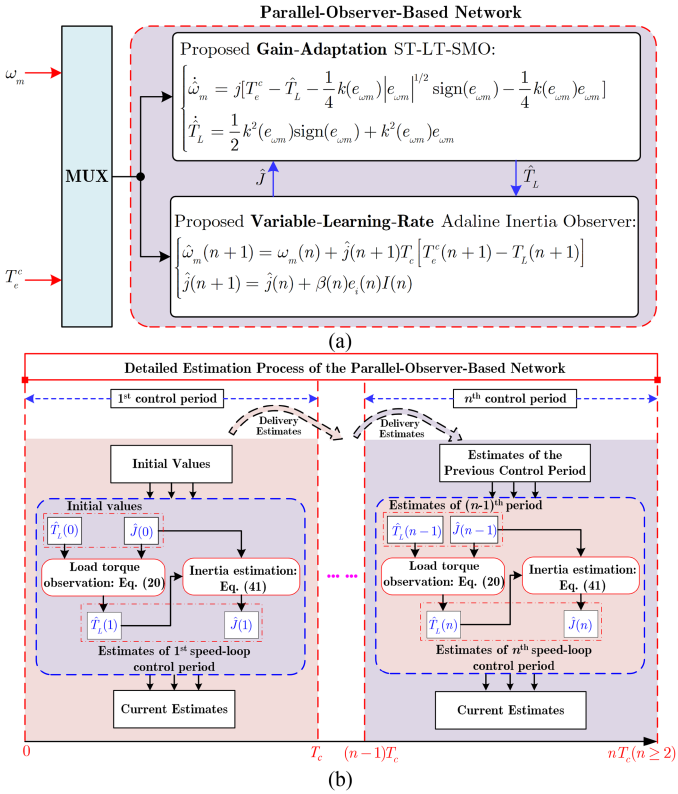

Fig. 6. Proposed parallel-observer-based network. (a) Schematic diagram. (b) Detailed parameter identification process of the parallel-observer-based network.

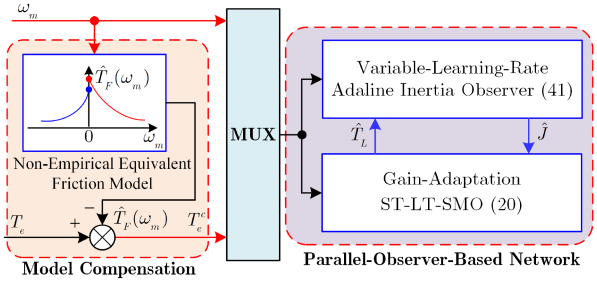

Fig. 7. Schematic diagram of the designed POBN-MC.

torque is usually present and variable, and the inertia may also vary).

As presented in Fig. 8, the first step aims to obtain an explicit mapping relationship between the nonlinear friction torque and the rotor speed. In order to reach this purpose, the detailed implementation process is described as follows. First, according to (13), the values of $\hat{f}_{cw}/J$ and $\hat{f}_{ccw}/J$ are acquired using the fitting results concerning the natural speed responses. Then, the relationship between these two values and the natural speed response ω_{md} is determined by building a lookup table, i.e., we have

$$\begin{cases} \frac{\hat{f}_{cw}}{J} = L_1(\omega_{md}), \text{when } \omega_{md} > 0 \\ \frac{\hat{f}_{ccw}}{J} = L_2(\omega_{md}), \text{when } \omega_{md} < 0 \end{cases} \tag{44}$$

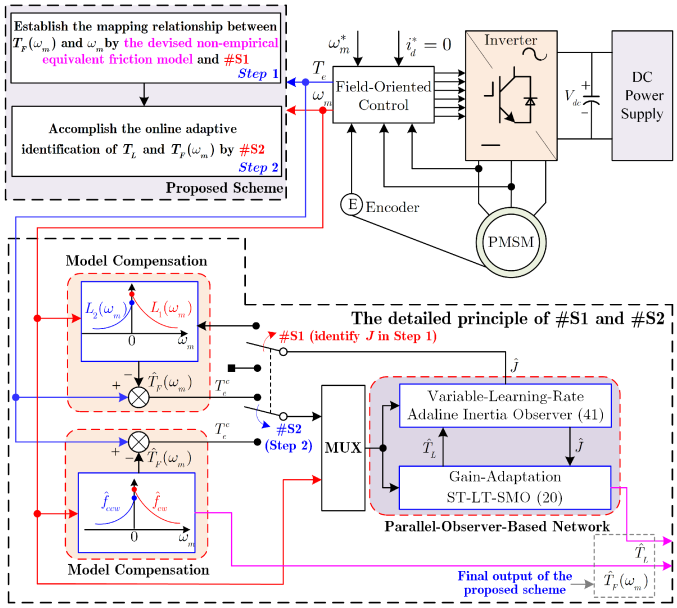

Fig. 8. Schematic diagram of the proposed scheme.

where $L_1(\cdot)$ and $L_2(\cdot)$ are the mapping relationships between $\hat{f}_{cw}/J$ and ω_{md} and between $\hat{f}_{cw}/J$ and ω_{md}, respectively. Actually, (44) implies that the values of $\hat{f}_{cw}/J$ and $\hat{f}_{ccw}/J$ corresponding to the actual rotor speed are $\hat{f}_{cw}/J = L_1(\omega_m)$ and $\hat{f}_{ccw}/J = L_2(\omega_m)$, respectively. Then, the #S1 part, as shown in Fig. 8, is performed to acquire the inertia. With (44) and the gained inertia information, the mapping relationship between the friction torque and the speed can be expressed as follows:

$$\hat{T}_F(\omega_m) = \begin{cases} \hat{J}\omega_m L_1(\omega_m), & \text{if } \omega_m > 0 \\ 0, & \text{if } \omega_m = 0 \\ \hat{J}\omega_m L_2(\omega_m), & \text{if } \omega_m < 0 \end{cases} \tag{45}$$

which ends the first step. The second step is intended to achieve the real-time identification of friction-and-load torque matching the real-time operating conditions, thereby accomplishing the target task of the proposed scheme. In this step, the nonlinear friction torque is calculated according to (45), and the load torque is obtained via the parallel-observer-based network, as shown in Fig. 8. Additionally, it is noticed that in the two steps, the parameter configurations with respect to the parallel-observer-based network can remain constant, i.e., achieving the two steps can utilize the same network.

Remark 5: Noticeably, in the first step of our scheme, the values of the orders r and h in (12) require to be determined in order to acquire the mapping relationship. Generally, the fitting error progressively decreases with increasing the polynomial order. It is worth noting that when the order increases to a certain value, the fitting error will be kept almost constant as the order increases [48], [49]. In Section IV, our experimental results also reveal this phenomenon. Actually, this phenomenon implies that the order at this time is high enough to yield a high-precision fitting result [48], [49]. If the order is further increased under this condition, the higher computational cost and even the overfitting will be incurred. In view of the above

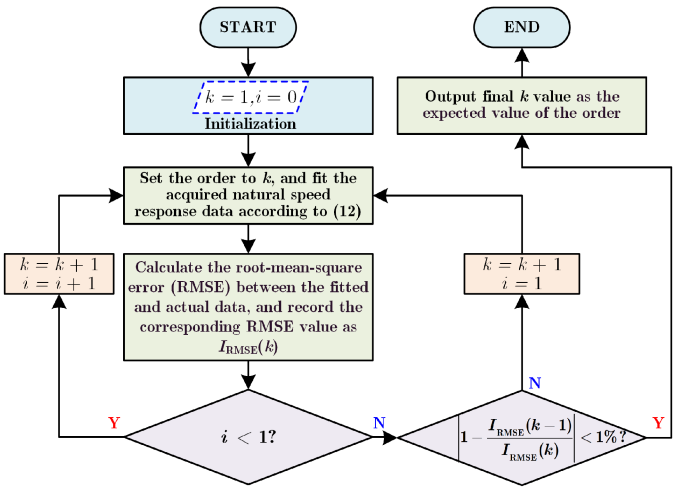

Fig. 9. Working schematic diagram of the proposed automatic-order-determination technique.

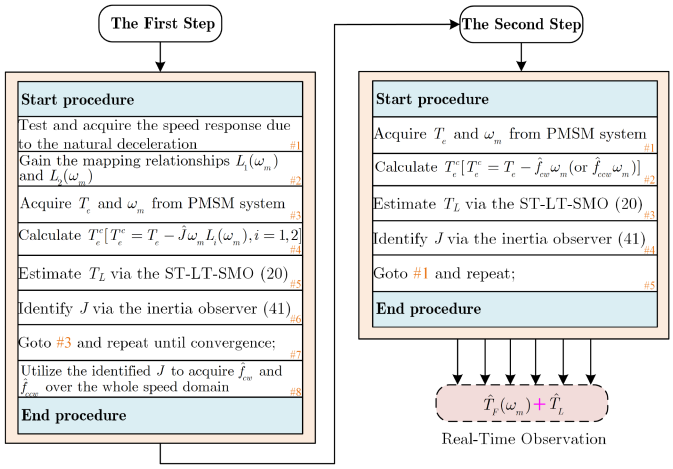

Fig. 10. Flowchart of the proposed scheme.

analysis, this article develops an automatic-order-determination technique, which uses the ratio between two root-mean-square error (RMSE) values as the judgment criterion to select an appropriate polynomial order. Fig. 9 shows the working schematic diagram of this proposed technique. With this method, r and h can be automatically assigned to desired values.

Remark 6: It should be noted that, in our proposed scheme, the acquired mapping relationship may differ from the actual one due to the existence of unconsidered factors (e.g., the speed measurement error). When such a case indeed occurs, the identified load torque is actually the sum of the load torque and the friction torque error, which has a corrective effect on the mapping relationship error. This does not imply, however, that separate identification is not necessary. In contrast, the separate-type identification can always significantly ease the identification burden, resulting in a more accurate aggregated estimate of the load and friction torque. Subsequent experimental results will confirm the above analysis.

Remark 7: Indeed, with the exception of the friction and load torque, the drive system suffers from unmodeled dynamics, which mainly comprise the deadtime effects, flux harmonics, cogging torque, and phase current measurement errors [50]. These unmodeled dynamics will result in a disturbance called the pulsating torque [51]. The pulsating torque usually exists in the form of different-order harmonics, and the frequency of the harmonics depends on the motor speed. Generally, the pulsating torque can be deemed to be a part of the load torque [51], [52]. In this article, the load torque is also essentially composed of two parts: one is the external load disturbance, and the other is the pulsating torque. This will be confirmed by experimental tests in Section IV.

In Fig. 10, the flowchart of the suggested scheme is given in detail. In the engineering practice, we can arbitrarily set the initial conditions $\hat{J}(0)$ and $\hat{T}_L(0)$ in the first step (Remark 4 indicates that $\hat{J}(0)$ and $\hat{T}_L(0)$ are able to be initialized by arbitrary values). For the second step, it is recommended to exploit the final estimation results of the first step as the initial conditions to facilitate practical applications. Additionally, it should be noted that the to-be-adjusted parameters of the proposed scheme only include η and β_0. The tuning guidelines are able to be concisely summarized as follows.

1) β_0 cannot be selected too small to seek a tradeoff between the parameter oscillations and the convergence rate.
2) A large η is conducive to reaching the condition (24) quickly and improving the convergence rate, and yet η is not supposed to be chosen so large as to aggravate the parameter oscillations.

The above-mentioned tuning guidelines are obtained from the tests of our scheme, which will be presented in Section IV.

IV. Simulation and Experimental Investigations

A. Simulation Investigation

1) Performance Tests for the Proposed Parallel-Observer-Based Network: As can be seen from Fig. 8, in the developed adaptive identification scheme, the two steps are both dependent on the use of the designed parallel-observer-based network. It is, therefore, necessary to evaluate the identification performance of this network. In the simulation, for ease, the friction model is modeled as (5), i.e., the Coulomb plus viscous friction model. Accordingly, the input T_e^c of the parallel-observer-based network is directly calculated using the established friction model. As shown in Table I, this article conducts the performance evaluation tests under four cases. The corresponding simulation results are displayed in Fig. 11. From there, it can be observed that whether both the load torque and inertia are variable or constant, or either of them is variable, the network is capable of tracking these two parameters accurately and quickly. Additionally, it is noticed from Fig. 11 that the time-variable gain function $k(e_{\omega m})$ can be automatically and quickly adjusted in accordance with the actual operating conditions. Consequently, the gain overestimation is eliminated, and the appropriate observer gains matching the working conditions are gained. This preliminarily confirms the effectiveness of the developed gain-adaptation mechanism.

TABLE I
SIMULATION SETUP AND CASES

Content		Description			
Simulation setup and initialization		$R_m = 0.867\ \Omega$, $L_d = L_q = 3.124$ mH, $P_n = 4$, $B_m = 0.0001$ N.m.s/rad, $C_m = 0.2$ N.m, $T_c = 200\ \mu$s, $\eta = 0.1$, $\beta_0 = 0.06$, $\hat{T}_L(0) = 0$ N.m, $\hat{J}(0) = 0.001$ Kg.m^2.			
Simulation cases		Case 1	Case 2	Case 3	Case 4
Given parameters	Ref. T_L	Fixed	Variable	Fixed	Variable
	Ref. J	Fixed	Fixed	Variable	Variable
Speed command given in the simulation		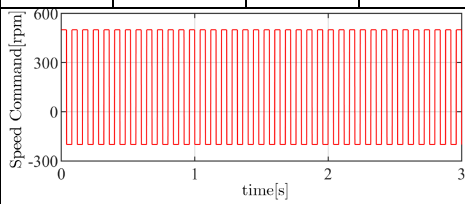			

Note: "Ref." denotes "Referenced".

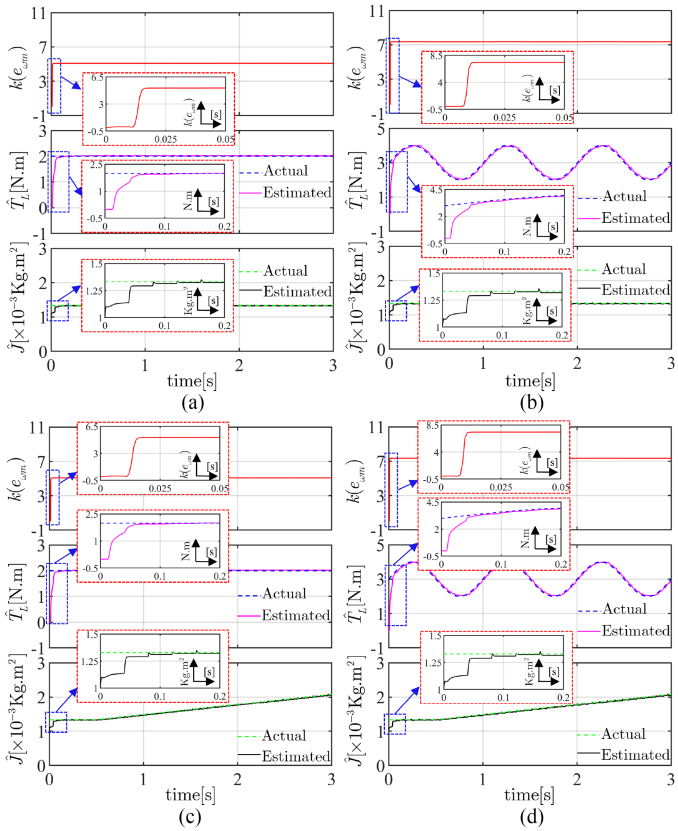

Fig. 11. Simulation results regarding the parallel-observer-based network. (a) Case 1. (b) Case 2. (c) Case 3. (d) Case 4.

If T_e rather than T_e^c is utilized directly as the input of the network (i.e., the model compensation part is disabled), then it is easy to know that the identified value of the load torque obtained from the parallel-observer-based network is essentially the lumped-identification result of the friction and load

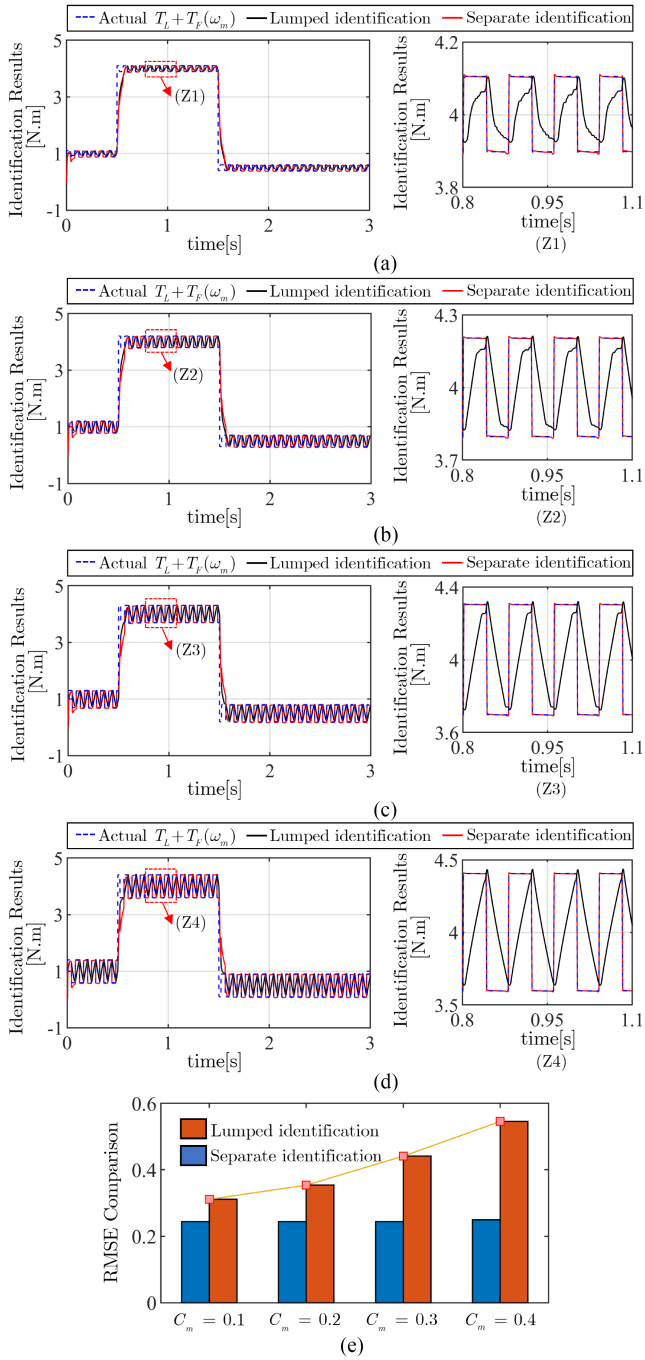

Fig. 12. Comparison of the separate and lumped identification. (a) $C_m = 0.1$. (b) $C_m = 0.2$. (c) $C_m = 0.3$. (d) $C_m = 0.4$. (e) RSME comparison.

torque. Fig. 12 exhibits some lumped-identification results under such a condition, and meanwhile, the corresponding separate-identification results are also given for comparison. Note that in the simulation, the estimated friction torque in the separation identification is directly calculated using the established friction model. Additionally, other simulation settings, except for the load condition, are consistent with Case 1. It can be seen from Fig. 12 that when performing the lumped identification for the friction and load torque, the estimated values are in poor agreement with the real value. By contrast, under different

TABLE II
PARAMETER CONFIGURATIONS OF DIFFERENT NOISE LEVELS

Noise Level	Block: Band-Limited White Noise		
	Noise power (Speed noise/Torque noise)	Sample time	Seed
Level 1	0/0	0.0001	23341
Level 2	$0.0001/0.5\times10^{-6}$	0.0001	23341
Level 3	$0.0003/1\times10^{-6}$	0.0001	23341

friction conditions, all the separate-identification results are of great match with the real value. The RMSE comparations in Fig. 12(e) also show the same phenomenon. Meanwhile, we can notice that the identification error becomes more pronounced with increasing the friction coefficient under the lumped identification. These experimental phenomena reveal that the lumped identification is difficult to gain high-precision estimation results (which coincides with the related analysis in Section I), indicating the need for the separate identification of the friction and load torque.

2) Antinoise Robustness Evaluation: As described in Section III, the proposed scheme is inseparable from the real-time rotor speed ω_m and electromagnetic torque T_e from the drive system, just as the other friction-and-load torque identification schemes (e.g., [9] and [15]). It should be pointed out that T_e and ω_m are unavoidably contaminated with the measurement noise in real-world applications. Here, to simulate this situation, this article utilizes the Simulink block "Band-Limited White Noise" to generate the measurement noise, as in the other literature (e.g., [53] and [54]). Then, the generated noise signal is superimposed on ω_m and T_e. In order to fully evaluate the robustness against noise, this article selects two existing friction-and-load identification schemes that belong to Type II (i.e., [24] and [26]) to compare with our scheme under three different noise levels. Table II presents the detailed parameter configurations of the Simulink blocks corresponding to the three noise levels. It is noted that in the tests, the friction torque is directly calculated using the established friction model, and other simulation settings, except for the load condition, are congruent with Case 1. Additionally, during the evaluation tests, the compared two techniques directly use the real inertia value for the estimation due to the lack of online inertia correction, while our scheme utilizes the real-time inertia-identification values. The comparison results are given in Fig. 13. From there, it can be observed that the estimation results from all three schemes are quite accurate in the absence of noise. However, in the presence of noise, the identification results from the schemes reported in [24] and [26] begin to fluctuate, and this phenomenon becomes increasingly evident as the noise level increases. Fortunately, Fig. 13 demonstrates that the presented scheme can still obtain stable and precise results (the gained results show only slight ripples) even when the drive system is severely contaminated by noise (e.g., at Level 3). Therefore, it can be concluded that our proposed scheme possesses superior noise immunity.

Remark 8: It is noted that for the sake of obtaining the real friction and load torque, the methods presented in [24] and [26] need to be slightly modified. To be specific, the actual

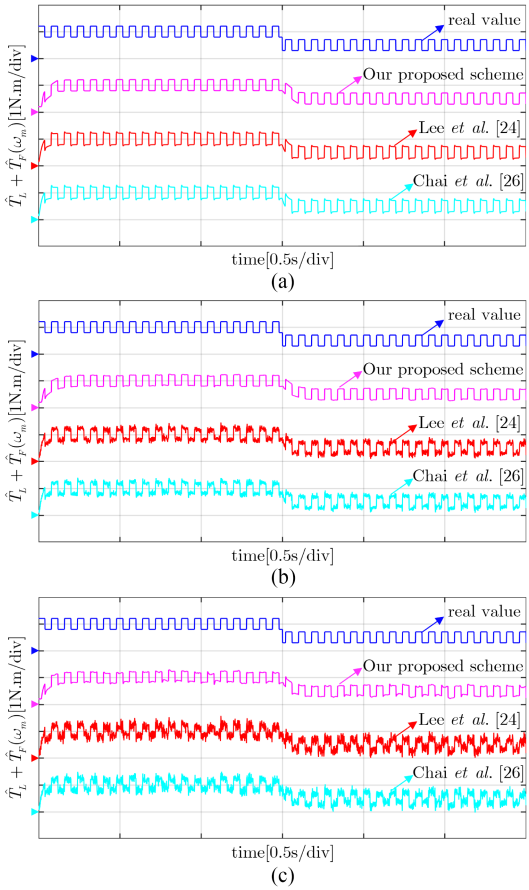

Fig. 13. Comparison of identification results under different noise levels. (a) At Level 1. (b) At Level 2. (c) At Level 3.

speed rather than the speed command is utilized to calculate the friction torque, and meanwhile, the involved friction model is incorporated into the torque signal channel of the corresponding load torque estimation technique in the feedforward manner, just as our proposed scheme. In the subsequent experiments, the same processing manner is adopted as needed when performing comparisons with some existing methods that belong to type II.

3) Additional Tests for the Proposed Inertia Observer: In Section III-C, a qualitative comparison concerning the presented inertia observer and the common online inertia estimation techniques has been offered. Here, some tests are performed to further evaluate the performance of the developed inertia observer. Specifically, under the three noise levels, as shown in Table II, the six common online inertia estimation techniques, as mentioned in Fig. 5, are used for comparison with the presented inertia observer. First, it should be pointed out that some inertia-identification techniques are implemented with the aid of the estimated information concerning the load and friction torque, just as the methods reported in [45] and [46]. Therefore, in order to ensure a fair comparison, the auxiliary estimation techniques that provide the necessary information for these inertia-identification algorithms should be considered in comparative tests. Table III gives the detailed parameter settings of the contrastive inertia-identification schemes during the tests (note that the parameters shown in Table III also contain the

TABLE III
PARAMETER SETTINGS OF INERTIA-IDENTIFICATION SCHEMES

Inertia-identification scheme	Detailed parameter configuration
EKF (see [41])	$P(0)=\text{diag}\{1,1,10\}, R=0.05,$ $Q(0)=\text{diag}\{10^{-5},10^{-5},0.1\}$
RLS (see [41])	μ=0.96, $P(0)=\text{diag}\{10^5,10^5\}$
MRAS (see [41])	$K_p=400, K_I=2$
ESMO [42]	$\kappa_0=0.005, K=-1000, f=0.3$
OPBM [43]	$\lambda=300$
FOEFDOPE [44]	$l=-0.06$

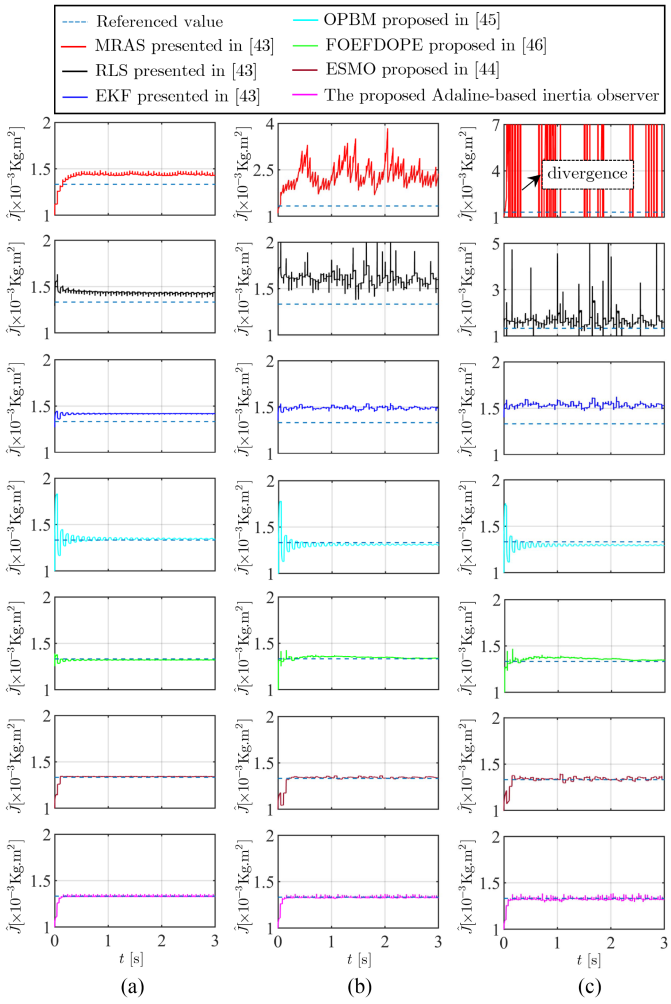

Fig. 14. Comparisons of seven inertia-identification techniques. (a) At Level 1. (b) At Level 2. (c) At Level 3.

parameters of the corresponding auxiliary estimation techniques). Additionally, other simulation settings are in-line with Case 2.

The comparison results are shown in Fig. 14. From Fig. 14(a), it can be observed that in the absence of noise, there is an obvious offset between the actual value and the identification values obtained from the MRAS, recursive least square (RLS), and EKF. One key reason for this phenomenon is that these

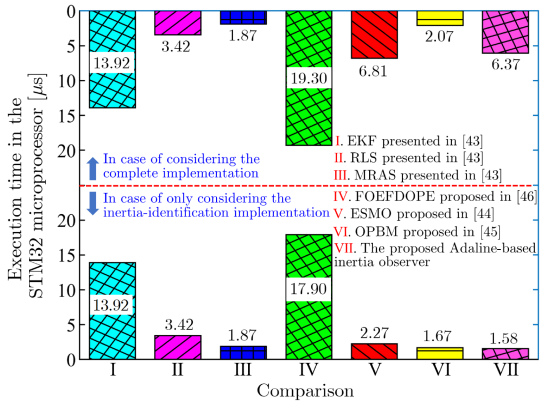

Fig. 15. Execution time comparison regarding different inertia-identification methods.

identification algorithms neglect the effects of friction and load torque on the inertia identification. Actually, since the existing inertia-identification algorithms are all devised based on a certain mechanical model [like (3)], ignoring the friction and load torque during the algorithm design will inevitably sacrifice the inertia-identification accuracy. In contrast, the other four schemes, including the proposed inertia observer, have accounted for the influence of friction and load torque so that they can yield more accurate results at Level 1, as shown in Fig. 14(a). In the presence of noise, it can be noticed from Fig. 14(b) and (c) that both the MRAS and RLS display a quite significant error due to poor robustness against noise. More seriously, Fig. 14(c) manifests that when the drive system is severely contaminated by noise at Level 3, the MRAS estimation result will fail to converge. Fortunately, compared with the MRAS and RLS, the other inertia-identification techniques obviously exhibit better noise-resistance capability, as shown in Fig. 14(b) and (c). Collectively, the comparison results fully indicate that the identification performance of our inertia observer is able to be comparable with the mainstream inertia-identification algorithms that possess excellent performance [such as the fixed-order empirical frequency-domain optimal parameter estimation (FOEFDOPE), orthogonal principle-based method (OPBM), and extended sliding-mode observer (ESMO)].

To more fully assess the performance and the application potential, the actual execution times of the proposed inertia observer and the six inertia-identification algorithms in the STM32F407 microprocessor are tested comparatively. Here, for a fair comparison, the execution time of the complete implementation is tested (i.e., the auxiliary estimation techniques that provide the necessary information for these inertia-identification algorithms are also considered). In addition, under the condition that only the inertia-identification part is considered, a comparison is also conducted accordingly. Fig. 15 exhibits the corresponding test results. From there, it can be observed that in the case of only considering the inertia-identification implementation, our method is the most competitive in terms of execution time (only around 1.58 μs). It is worth noticing that the execution time of our method is even slightly lower than

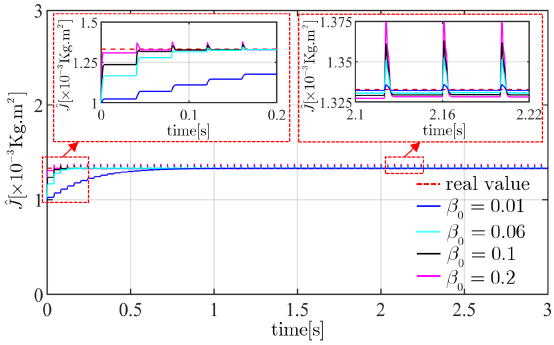

Fig. 16. Influence of β_0 on inertia observation.

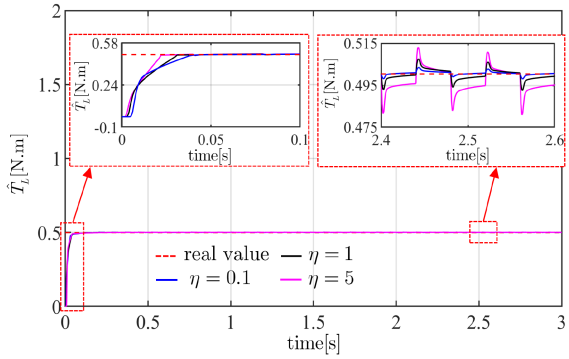

Fig. 17. Influence of η on load torque identification.

the MRAS and the OPBM (these two techniques are known for their low computational burden). Moreover, Fig. 15 indicates that in the case of considering the complete implementation, the proposed inertia observer has a mitigated computational cost compared with the FOEFDOPE and the ESMO. (Note that these two schemes are more competitive among the mentioned six common inertia-identification algorithms due to the fact that they possess no less than four virtues described in Fig. 5 and are not restricted by operating conditions.) That is to say, the presented inertia observer is able to have a competitive computational burden while maintaining more advantages. Overall, the superiority of the developed inertia observer is fully highlighted by the results from Figs. 5, 14, and 15.

4) Influence of η and β_0 on Estimation Performance: As mentioned previously, the proposed adaptive identification scheme possesses two to-be-adjusted parameters (i.e., η and β_0). The parameters η and β_0 belong to the ST-LT-SMO (20) and the inertia observer (41), respectively. Here, this article offers a detailed discussion with regard to the impacts of the parameter configuration on the identification performance of these two observers. Note that in related tests, the speed command is aligned with that in Case 1.

First of all, the developed inertia observer is individually tested with different β_0 values. The corresponding results are shown in Fig. 16. Note that during the test, the load torque is configured as $T_L = 0\,\mathrm{N}\cdot\mathrm{m}$. From Fig. 16, we can draw the conclusion that with β_0 increases, the presented inertia observer's convergence rate will become faster, and yet the parameter oscillations may be exacerbated. Second of all, a separate test concerning the proposed ST-LT-SMO is performed to evaluate the effect of the value of η. Note that, in the test, the inertia J is set as its true value. Fig. 17 exhibits the impacts of different η values on the load torque identification results. Notably, it can be seen from (21) that the larger the η is, the faster the adaptive function $k(e_{\omega m})$ grows, which is more beneficial for fulfilling the condition (24). Nevertheless, Fig. 17 indicates that a large η will aggravate the parameter oscillations. Additionally, Fig. 17 demonstrates that the value of η has an effect on the convergence rate, i.e., the convergence rate will be accelerated as η increases. The above conclusions provide some simple guidelines for tuning η and β_0 in practical applications.

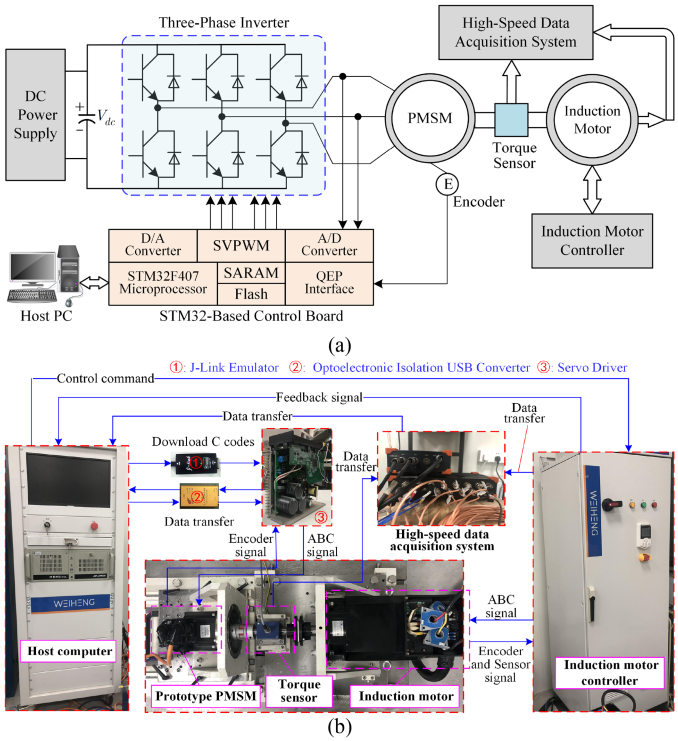

Fig. 18. Test system. (a) Configuration and principle of the overall test system. (b) Photograph of the test system.

B. Experimental Investigation

1) Test System Configuration and Parameter Settings: The suggested scheme is validated on a built test system, which is shown in Fig. 18. The established experimental system mainly comprises the following parts:

1) a self-developed servo driver embedded with an STM32F407 microprocessor (168 MHz CPU/210 DMIPS);
2) a host computer used for code programming and data observation;
3) a parameter identification platform, including a 0.78-kW prototype PMSM, a high-precision torque sensor, a 7.5-kW induction motor, and a high-speed data acquisition system (which is the Sirius Dewesoft with 16 channels).

TABLE IV
SPECIFICATION OF THE TEST SYSTEM

Parameters	Values/Units
Rated torque	5 N.m
Rated current	5 A
Pole pair	4
q-axis inductance	3.124 mH
d-axis inductance	3.124 mH
Stator resistance	0.867 Ω
Rotor inertia (PMSM)	1.333×10^{-3} Kg.m^2
Total inertia	0.0199 Kg.m^2
Allowable maximum speed of the system	1500 rpm
The inverter's switching frequency	10 kHz
Encoder resolution (incremental)	2500 p/r

```
int main(void)
{
   Disable CPU interrupt and reset all interrupt flags;
   STM32 HAL library initialization;
   System clock configuration;
   GPIO initialization;
   Servo parameters initialization;
   Encoder initialization;
   ADC initialization;
   DAC initialization;
   Serial communication interface configuration;
   Timer initialization;
   PWM initialization;
   Enable global interrupt;
void interrupt_handler(void){
   Enable PWM interrupt routine;
   Acquire encoder feedback position;
   Calculate the rotor speed;
   Speed control adjustment;
   Measure phase currents;
   Clark and Park transformations;
   Execute the proposed adaptive identification scheme;
   Current control adjustment;
   Inverse Park transformation;
   SVPWM update;
  }
}
```

Fig. 19. Complete implementation flowchart of *C* codes concerning employing the proposed scheme.

The detailed specification regarding the experimental system is listed in Table IV. It is noted that the load torque is generated by the induction motor, driven by an industrial voltage-source inverter (VSI) set for torque control. The prototype PMSM employs the FOC with $i_d^* = 0$, as depicted in Fig. 1. Additionally, in the built test system, all the sensors are connected to the high-speed data acquisition system so that the signals (such as the actual load torque generated by the induction motor) can be accurately measured.

Furthermore, it should be mentioned that the experimental system utilizes the IAR embedded workbench (v8.3) software as a code composing tool. Under this programming environment, the *C* codes are compiled and then downloaded to the STM32-based control board through the J-link emulator. Fig. 19 displays the complete implementation flowchart of *C* codes concerning employing the proposed friction-and-load identification scheme. In order to transfer and receive the data between the STM32-based control board and the host computer, the optoelectronic isolation USB converter (USB to RS232/485) and the software named servo tuning platform (STP) are used as a real-time transfer device and a hardware management software, respectively. With the aid of the transfer device, the real-time data of the observed variables (such as the rotor speed and the identified load torque) can be transmitted to the STP for immediate display. At the same time, the parameters, such as control flags and controller gains, are able to be configured using the STP and then updated to the control board through the transfer device.

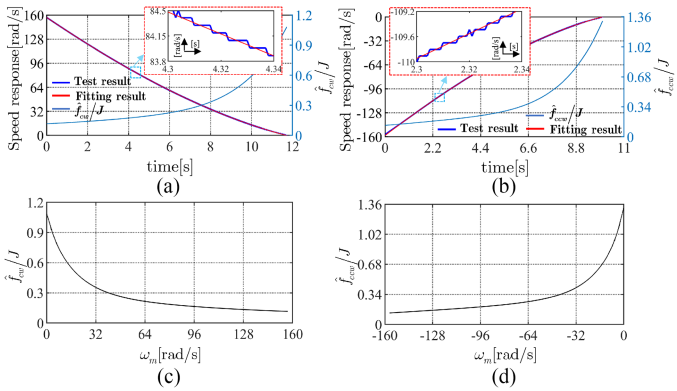

Fig. 20. Speed responses caused by the natural deceleration. (a) and (b) are the test results under forward and reverse rotation, respectively. (c) Mapping relationships between $\hat{f}_{cw}/J$ and ω_m. (d) Mapping relationships between $\hat{f}_{ccw}/J$ and ω_m.

Additionally, it is noted that, in the subsequent experiments, the POBN-MC is designed with $\eta = 0.3$ and $\beta_0 = 0.005$ in order to achieve relatively good identification performance.

2) Natural Speed Response Test and Equivalent Friction Factor Determination: Here, the speed responses due to the natural deceleration in the PMSMs two rotation directions are first acquired so as to achieve the first step of our proposed scheme. Fig. 20 exhibits the corresponding test results and the curve fitting results regarding the natural speed responses. With the fitting results and using (13), we can derive the function relationships between $\hat{f}_{cw}/J$ and t_1 and between $\hat{f}_{ccw}/J$ and t_2, as shown in Fig. 20(a) and (b). Then, the mapping relationships between $\hat{f}_{cw}/J$ and ω_m and between $\hat{f}_{ccw}/J$ and ω_m can be obtained, as displayed in Fig. 20(c) and (d).

Next, in order to determine the two equivalent friction factors, inertia information needs to be provided. As shown in Fig. 8, with aiding from the #S1 part, the inertia can be acquired in the first step of the suggested scheme. Fig. 21 displays the related identification results obtained in the first step. It should be stressed that, as described in Section III-D, the first step is utilized during the system commissioning. Therefore, no load torque is generated during the experiments corresponding to Fig. 21. Additionally, in Fig. 21, the experiments are conducted under both the unidirectional and bidirectional speed conditions in order to enable the test results to be more compelling. We can see from Fig. 21 that the identified inertia is around $0.02012\,\mathrm{kg}\cdot\mathrm{m}^2$ for all tests, which is rather close to its actual value given in Table IV (only about 1.11% error). Meanwhile, it can be noticed that the estimated load torque $\hat{T}_L$ converges to near zero, which is in a good accord with the actual situation. It should be

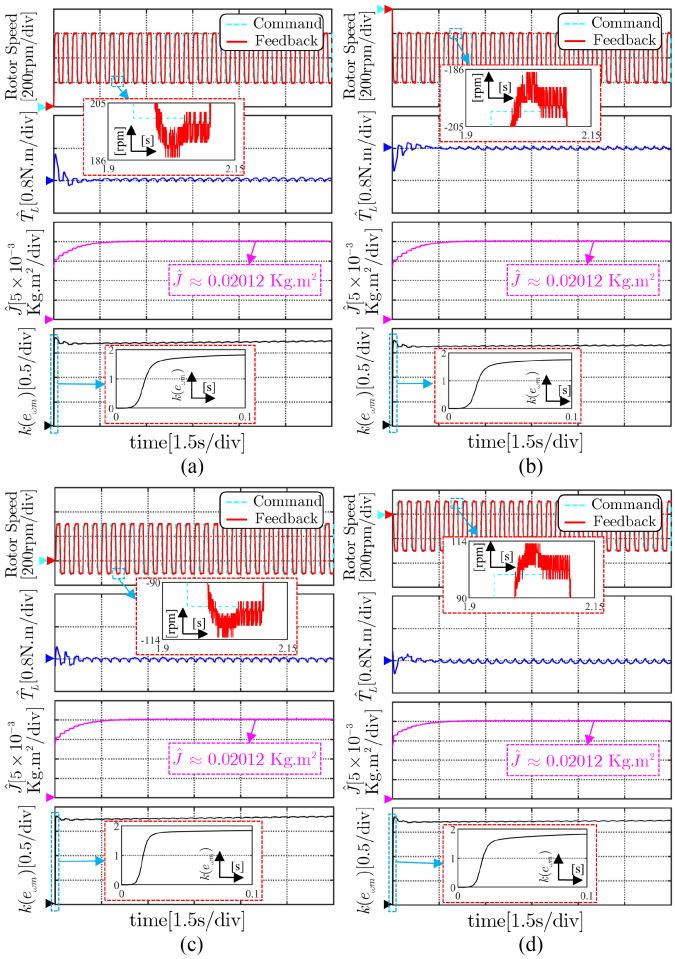

Fig. 21. Related identification results that are acquired in the first step. (a) and (b) are the test results under unidirectional speed conditions. (c) and (d) are the test results under bidirectional speed conditions.

noted that this experimental phenomenon implies that the model compensation part is accurately able to counteract the nonlinear friction torque (i.e., the precise friction modeling is achieved). Additionally, it is observed that the designed time-variable gain function $k(e_{\omega m})$ can be adjusted quickly, which ensures that the four observer gains have appropriate values matching the real-time operating condition.

According to the results from Figs. 20 and 21, the mapping relationships between $\hat{f}_{cw}$ and ω_m and between $\hat{f}_{ccw}$ and ω_m are able to be easily obtained, which are shown in Fig. 22. From there, it is not difficult to find that the two equivalent friction factors are inconsistent, which means that the friction torque over the whole speed domain is asymmetric. In addition, it can be noticed that the two friction factors are the nonlinear functions of the speed ω_m. Namely, the friction torque varies nonlinearly with the rotor speed. With the above experiments, the first step of our suggested scheme has been fully implemented.

Remark 9: In the first step of our developed scheme, the orders of the polynomials $p(t_1)$ and $q(t_2)$ require to be assigned. Using the automatic-order-determination technique developed in Fig. 9, the values of the orders r and h in (12) are determined as $r = 5$ and $h = 4$, respectively. Here, taking the value of the order

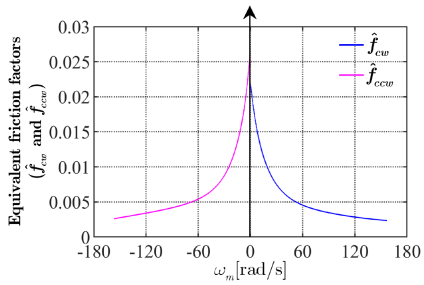

Fig. 22. Mapping relationships between $\hat{f}_{cw}$ and ω_m and between $\hat{f}_{ccw}$ and ω_m.

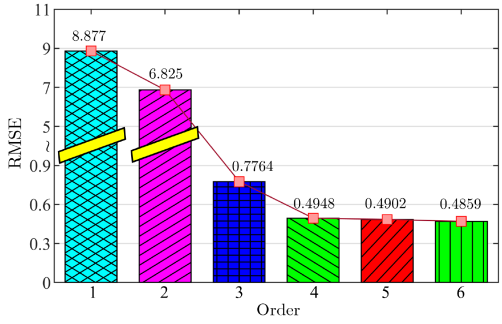

Fig. 23. Fitting error comparison of the different-order polynomials.

r as an example, we conduct some tests to assess the plausibility of $r = 5$. The test results are shown in Fig. 23, where the fitting errors under the different-order polynomials are evaluated. From there, we can observe that the RMSE decreases with increasing the order, which means that the fitting result is increasingly accurate. Moreover, it can be found that the decrease of the RMSE is already less apparent when the order exceeds four. Meanwhile, we can notice that when the order is chosen as five, the judgment criterion in Fig. 9 has been satisfied. According to these experimental phenomena, it can be known that the value of r determined by the proposed automatic-order-determination technique is appropriate, which confirms the validity of the developed technique. At the same time, the relevant analysis in Remark 5 is confirmed by the above phenomena.

3) Performance Evaluation Concerning the Load Torque Tracking Capability for the Second Step of the Proposed Scheme: Here, several real-time experiments are carried out to evaluate the load torque tracking performance with respect to the second step of our scheme. Fig. 24 gives the experimental results under variable-speed conditions. Notice that in the experimental results of Fig. 24, the actual T_L is obtained by the high-speed data acquisition system. This is also true for subsequent figures. From Fig. 24, it can be easily observed that the second step of the suggested scheme can track the variable load torque with high accuracy under different load conditions. These experimental phenomena indirectly demonstrate that the nonlinear friction torque has been accurately compensated, which implies that our scheme can exactly acquire real-time load-and-friction information. Moreover, it is noticed that the designed time-variable gain function $k(e_{\omega m})$ can be adaptively adjusted to match the real-time operating conditions, laying the foundation for the

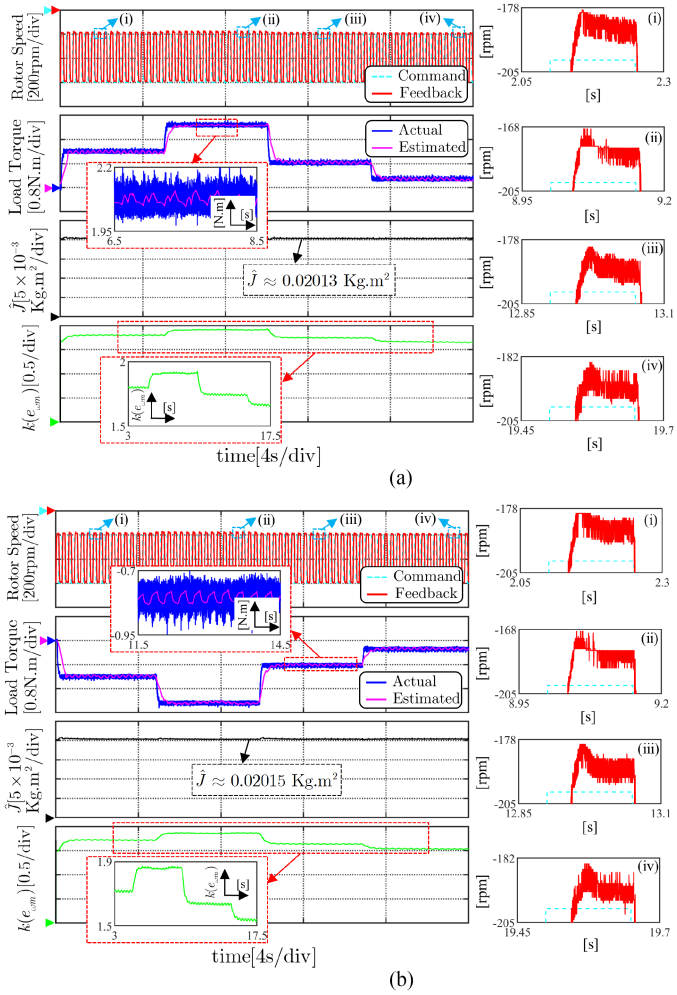

Fig. 24. Load torque tracking capability evaluation under the variable-speed condition. (a) Apply a positive time-varying load torque. (b) Apply a negative time-varying load torque.

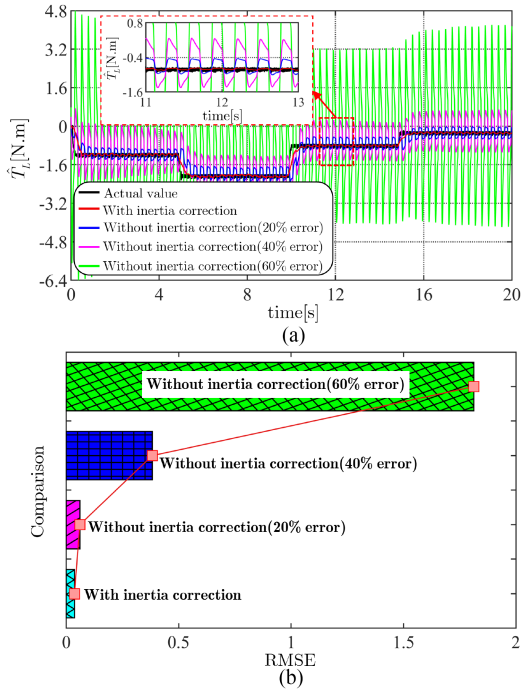

Fig. 25. Influence of different inertia errors on the load torque identification. (a) Load torque estimation results under different inertia errors. (b) RMSE comparison.

developed ST-LT-SMO to obtain appropriate gains. It should be pointed out that the exact $\hat{J}$ provided by the inertia observer is also one of the factors for obtaining accurate $\hat{T}_L$. Fig. 25 manifests the negative influence of different inertia errors on the load torque identification under the condition that the proposed inertia observer is disabled (i.e., the inertia correction is not conducted). Note that in the experiments corresponding to Fig. 25, the speed command aligns with that in Fig. 24. From Fig. 25, it can be observed that as the inertia error increases, the identification accuracy of the load torque becomes increasingly poor. In fact, based on the mechanical model (3), it can be derived that when there is an error in the inertia (assume that J_{error} stands for the inertia error), the actual load torque is $T_L + J_{\text{error}}\dot{\omega}_m$, which implies that the actually identified load torque will be close to this value. This is the pivotal cause of the load torque identification error appeared in Fig. 25. The phenomenon from Fig. 25 confirms the critical role of inertia correction in the exact load torque identification. It is for this reason that numerous existing load torque identification methods (such as [32] and [55]) take the online inertia identification into account.

Remark 10: From Fig. 24, it can be observed that the actually identified load torque exhibits slight fluctuations. The possible reasons include at least: first, the influence of η value. The greater η means the more pronounced fluctuation in the identification result, as shown in Fig. 17. This is the main cause of the fluctuations in the identification result. Second, the influence of the mapping relationship error. As pointed out by Remark 6, the actually identified load torque may contain the friction torque error. If this indeed occurs, the identification result can also produce some fluctuations.

Fig. 24 has evaluated the load torque tracking ability with respect to the second step of the presented scheme under the variable-speed condition. Here, in order to further assess the performance, this article tests the load torque tracking performance of the second step under the constant-speed condition. Fig. 26 exhibits the corresponding test results. Of note, the inertia identification has no meaning at a constant speed [34]. It is for this reason that the inertia-identification value is unable to be updated during the constant-speed operation. This implies that the developed parallel-observer-based network actually becomes an SO-SMO to observe the load torque. Therefore, in Fig. 26, we do not show the corresponding inertia-identification result. In addition, it should be pointed out that the influence of inertia on load torque identification is practically negligible during the constant-speed operation because the inertia torque term $J\dot{\omega}_m$ is almost zero. The results from Fig. 26 indicate that the second step of the proposed scheme can still track the changing load torque with high precision under the constant-speed condition. Meanwhile, we can also observe that the time-variable gain function $k(e_{\omega m})$ is automatically adjusted in accordance with

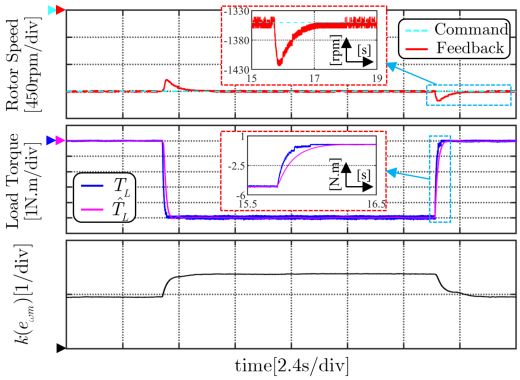

Fig. 26. Load torque tracking capability evaluation under the constant-speed condition.

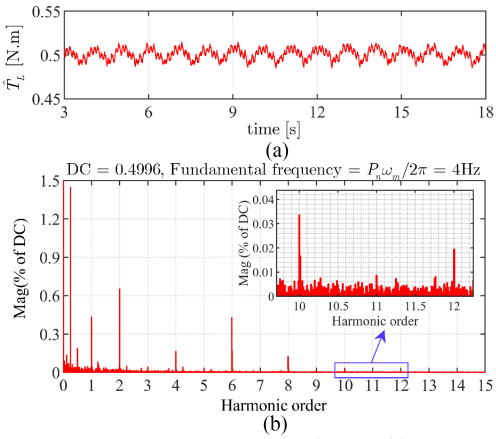

Fig. 27. Experimental results at $60\,\mathrm{r/min}(2\pi\,\mathrm{rad/s})$. (a) Identified load torque. (b) Frequency spectrum of the identified load torque.

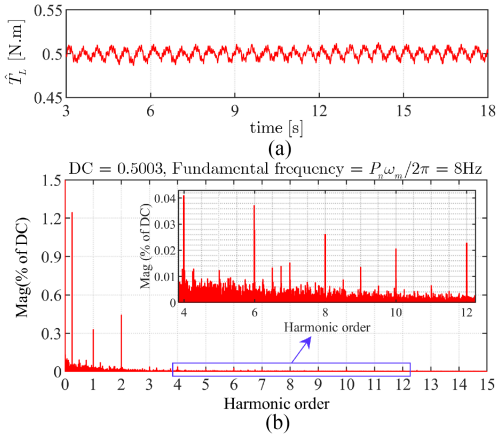

Fig. 28. Experimental results at $120\,\mathrm{r/min}(4\pi\,\mathrm{rad/s})$. (a) Identified load torque. (b) Frequency spectrum of the identified load torque.

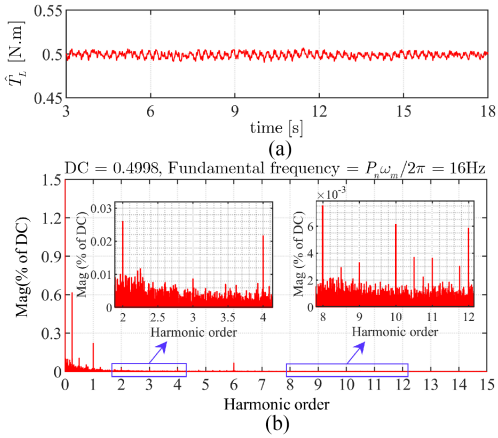

Fig. 29. Experimental results at $240\,\mathrm{r/min}(8\pi\,\mathrm{rad/s})$. (a) Identified load torque. (b) Frequency spectrum of the identified load torque.

the real-time operating conditions, which once again confirms the effectiveness of the designed gain-adaptation mechanism.

Overall, our scheme is accurately capable of identifying the load torque under both the variable and constant speeds, which implies that the corresponding friction torque is compensated well. In other words, the proposed scheme can serve its purpose of acquiring accurate friction-and-load knowledge.

4) Analysis and Assessment on the Components of the Actually Estimated Load Torque: As described in Section III-D, the identified load torque consists actually of two parts, i.e., the external load disturbance and the pulsating torque. Here, this article utilizes the proposed adaptive ST-LT-SMO to conduct experimental tests to analyze and evaluate the components of the actually estimated load torque. In order to clearly demonstrate the harmonic components, the relevant experiments are carried out for several constant speeds: $60\,\mathrm{r/min}$, $120\,\mathrm{r/min}$, and $240\,\mathrm{r/min}$. Additionally, in the experiments, a 0.5-N·m constant load generated by the induction motor is applied to the motor shaft, and the inertia value of the proposed ST-LT-SMO is set as the real value given in Table IV. Figs. 27–29 show the identification results of the load torque in the time span [3,18] and the corresponding Fourier analysis results. Note that for the purpose of clarity, we only give the harmonics in the range from 1st to 15th. From Figs. 27 to 29, it can be observed that the following harmonics are relatively prominent in all experimental results: 1st, 2nd, 4th, 6th, 8th, 10th, and 12th. According to Niewiara et al. [51], we can deduce the source of these harmonics as follows.

1) The 1st- and 2nd-order harmonics are mainly caused by the phase current measurement errors.
2) The 6th- and 12th-order harmonics principally result from the flux harmonics and deadtime effects.
3) The other-order harmonics are tightly related to the cogging torque.

The above test results confirm that the proposed ST-LT-SMO can effectively identify the harmonic components associated with the pulsating torque, providing further evidence for the validity of our developed load torque observer.

5) Performance Comparison With Previous Works: As described in Section I, the existing friction-and-load identification techniques can be divided into the lumped type, Type I, and Type II (note that the latter two types belong to the separate-type identification). Here, we select the SMO [9] and the DOB [10] as the representative techniques of the lumped type, and meanwhile, the schemes reported by Zuo et al. [15] and Lin [19] are chosen

TABLE V
DETAILED PARAMETER SETTINGS OF COMPARISON SCHEMES

Comparison scheme	Detailed parameter configuration
Zhang et al. [9]	$\eta = -1000, g = 3$
Ohnishi et al. [10]	$k_1 = 10000, k_2 = 200$
Zuo et al. [15]	$k_1 = 200, k_2 = 10000, k_a = 1.5, k_b = 120000$
Lin [19]	α=0.92, $P(0) = \text{diag}\{10^5, 10^5\}$
Lee and Tomizuka [24]	$\tau = 0.01$

as the representative methods in the existing Type I. The method proposed by Lee and Tomizuka [24] is selected as the typical method of the current Type II. Thus, a total of five previously reported friction-and-load approaches are utilized to compare with our suggested scheme. It is noted that during contrast tests, the techniques that ignore inertia mismatch directly use the real inertia value, while the methods that consider the inertia correction utilize the real-time inertia-identification values. Additionally, for a fair comparison, the related parameters of the above-mentioned schemes are specially chosen so as to gain convergence rates relatively consistent with our developed scheme. Table V gives the detailed parameter values of these comparison schemes. Note that, during the contrast experiments, three load cases are tested as follows.

Test 1: Applying a time-varying load torque.
Test 2: Applying a 1-N·m constant load torque.
Test 3: Applying a 4.5-N·m constant load torque.

In the experiments, the speed command is in-line with that in Fig. 24. Fig. 30(a) displays the comparison results regarding the identified values obtained by our scheme and the five existing methods under Test 1. It is not difficult to find that the aggregated value of $\hat{T}_L$ and $\hat{T}_F(\omega_m)$ estimated by the suggested scheme is in much better agreement with the actual value. This experimental phenomenon highlights the superior real-time observation performance of our scheme. Fig. 30(b) compares the RMSE between the identified and actual values under the three load cases. It can be seen from there that the suggested scheme possesses a competitive identification accuracy over the contrastive techniques in all load cases. It should be pointed out that both the presented scheme and the method reported by Lee and Tomizuka [24] belong to Type II, and hence, it is not difficult to understand that their estimation performance outperforms the lumped type and Type I. With respect to the reasons why the accuracy of our proposed scheme is superior to that of the scheme developed in [24], our explanations are as follows.

1) Our scheme can adaptively tune the gains of the load torque observer to match the real-time working conditions.
2) The load torque estimation involved in the suggested method is implemented by developing an SO-SMO, which has better antinoise robustness than the DOB, which is used to identify the load torque in [24].
3) The nonempirical equivalent friction model involved in our scheme avoids additional accuracy uncertainty.

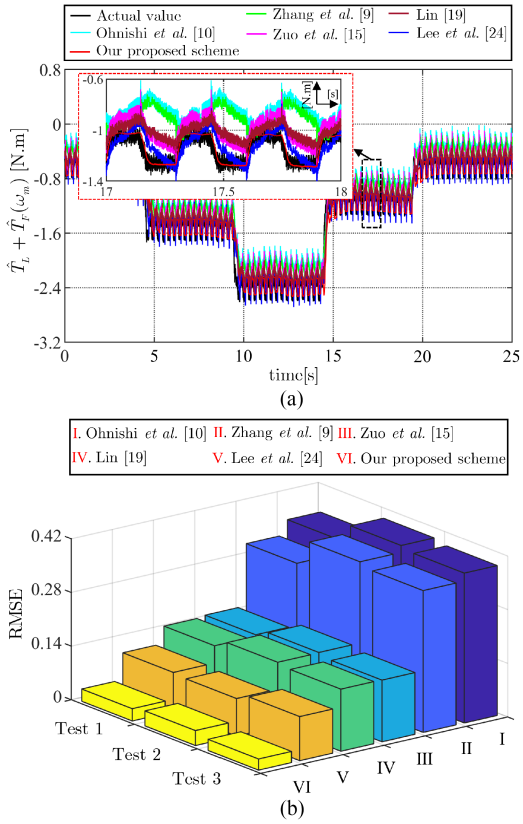

Fig. 30. Performance comparisons with existing works. (a) Comparisons of identification results. (b) RMSE comparison.

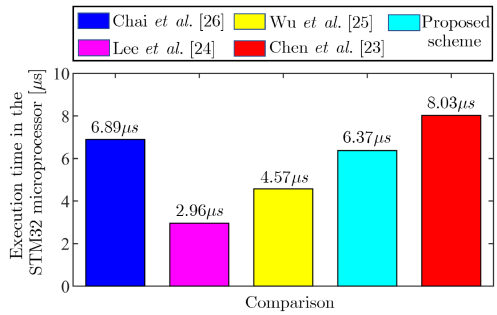

Fig. 31. Execution time comparison of our proposed scheme with the methods reported in [23], [24], [25], and [26].

6) Comparison of the Execution Time: In order to further highlight the superiority of our developed scheme, the execution time in the STM32 microprocessor is compared between our scheme and four existing friction-and-load methods that belong to Type II (i.e., [23], [24], [25], and [26]). Fig. 31 demonstrates the comparison results. It can be easily observed that the computational burden of the proposed scheme is not the lowest, but it is also not the highest. It should be noted that, compared with these several existing methods belonging to Type II, the advantages of our scheme are reflected in the following aspects.

1) It provides a simpler and more high-efficient technique for accurate friction modeling via developing a nonempirical equivalent friction model.

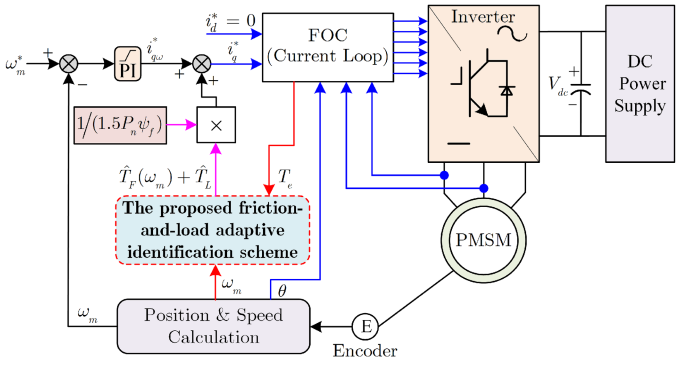

Fig. 32. Control block diagram of the simple application case.

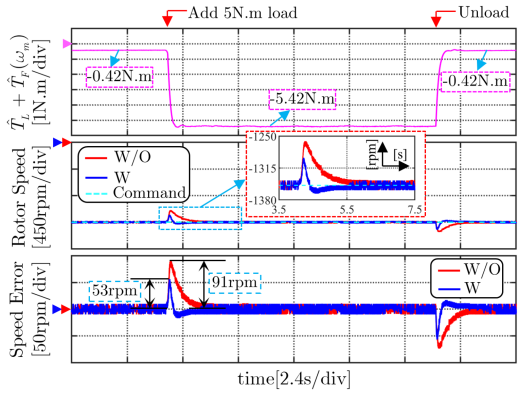

Fig. 33. Experimental results of the simple application case under the constant-speed condition.

2) It offers a highly competitive load torque identification scheme and realizes the adaptive load torque identification.
3) Identification process does not suffer from the inertia mismatch.

Hence, we can draw the conclusion that the proposed scheme has significant superiority while providing a moderate computational cost.

7) Control Effects Test Based on a Simple Application Case: Here, a simple application case regarding the suggested scheme is offered to confirm the potential benefits brought about by the accurate friction-and-load identification. In this application case, the identified T_L and $T_F(\omega_m)$ are utilized for feedforward compensation to enhance the speed control behavior of the PMSM-drive system against load variations and friction. Under this condition, the q-axis current command is able to be expressed as $i_q^* = i_{q\omega}^* + [\hat{T}_L + \hat{T}_F(\omega_m)]/[1.5P_n\psi_f]$ [41], where i_q^ω denotes the output of the speed controller. Fig. 32 depicts the control block diagram of this simple application case.

Here, the control effect test experiments are performed under both constant- and variable-speed commands. Fig. 33 presents the experimental results under the constant-speed condition (note that "W" represents "with feedforward compensation," and "W/O" stands for "without feedforward compensation"). It should be pointed out that, similar to Fig. 26, we do not give the inertia-identification result under the constant speed

TABLE VI
PERFORMANCE COMPARISON WHEN APPLYING DIFFERENT LOAD-AND-FRICTION IDENTIFICATION SCHEMES

Indicators / Applied schemes in FC	MSE/[rpm]	ASE/[rpm]	RMSE
Zhang et al. [9]	425	4.1908	109.1065
Ohnishi et al. [10]	427	4.3087	110.6754
Zuo et al. [15]	419	2.9908	103.9256
Lin [19]	419	3.0971	104.1130
Lee and Tomizuka [24]	413	2.1431	101.3564
The suggested scheme	403	1.2019	98.1428

Note: "FC" stands for "feedforward compensation".

(refer to the related description regarding Fig. 26 for a detailed explanation). It can be observed from Fig. 33 that when the PMSM-drive system encounters the load variation, the actual speed will generate a significant fluctuation. Fortunately, when applying the proposed scheme in the feedforward compensation, the fluctuation will be significantly diminished (Fig. 33 indicates that the amplitude of fluctuation is reduced approximately $38\,\mathrm{r/min}$ in the case of adding 5-N·m load). Clearly, the drive system gains a good antidisturbance ability when applying our scheme.

Fig. 34 shows the experimental results under the variable-speed condition. In Fig. 34, comparing the positions (i) and (iv), it can be observed that the actual speed at the position (iv) is significantly closer to the command speed (we can find that the corresponding speed error is apparently smaller). Since the operating conditions corresponding to the positions (i) and (iv) are both no-load, the obtained $\hat{T}_L + \hat{T}_F(\omega_m)$ at this time is actually the friction torque of the drive system. From this, it follows that the speed error caused by the friction torque is suppressed. Comparing the positions (i) and (ii), we can see that when the load torque is applied to the drive system, the speed-tracking error is obviously increased, which means that the speed control performance further deteriorates. Fortunately, the speed-tracking error can be diminished by activating the feedforward compensation, which indicates that the friction and load torque are well counteracted. Additionally, comparing the positions (iii) and (iv), it can be noticed that in the case of enabling the feedforward compensation, even if the load changes, the corresponding speed-tracking error is virtually unaffected. This experimental phenomenon implies that the adverse effect of load variation on the speed is restrained in time by the feedforward compensation. The above phenomena fully demonstrate that applying the proposed scheme to the feedforward compensation is clearly able to weaken the influence of friction and load torque.

Furthermore, based on this simple application case, this article also evaluates the control effects of applying other friction-and-load identification schemes (i.e., the five methods that are previously compared with our scheme, including [9], [10], [15], [19], and [24]). Note that the experimental settings are in agreement with those in Fig. 34. The related test results are summarized in Table VI, where various performance

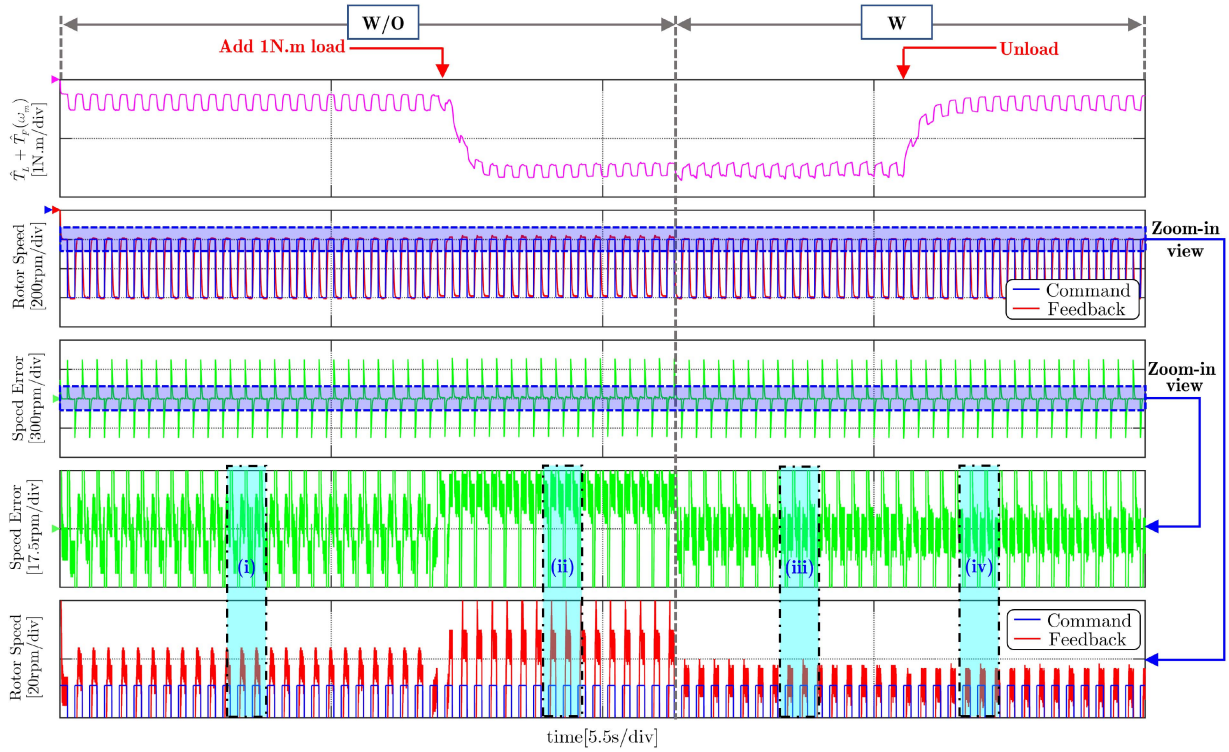

Fig. 34. Experimental results of the simple application case under the variable-speed condition.

indicators, including maximum speed error (MSE), average speed error (ASE), and RMSE value between the reference and actual speed, are compared to assess the performance of applying different friction-and-load estimation methods in the feedforward compensation. Clearly, we can see that the drive system attains better speed-tracking ability when applying the suggested scheme, which benefits from the superior identification quality of our scheme over other friction-and-load identification schemes, as pointed out by Fig. 30.

A fairly simple application case concerning the suggested scheme is reported above. Introducing such a simple application case aims at further evaluation of the effectiveness and feasibility of the proposed scheme. It should be pointed out that apart from disturbance compensation, our scheme can also be applied in monitoring friction, tuning the speed loop, optimizing advanced control strategies (such as model predictive and sliding-mode control), etc. Future work will explore more engineering cases of the suggested scheme.

V. Conclusion

In this work, an adaptive identification scheme with a two-step mechanism is presented to acquire the nonlinear friction torque and the unknown load torque online and accurately. The two-step identification mechanism is derived from the devised POBN-MC, which is composed of two parts connected together. One is a parallel-observer-based network formed based on the proposed gain-adaptation ST-LT-SMO and variable-learning-rate Adaline inertia observer. The other is a model compensation part constructed using the developed nonempirical equivalent friction model. With ingenious designs, the estimation errors of the inertia and the load torque are both governed to converge to zero over time. In comparison with the existing friction-and-load identification techniques, our proposed scheme is capable of capturing the friction-and-load information in a manner that integrates both accuracy and simplicity. Additionally, it should be underscored that our scheme offers newly available techniques in friction identification, load torque observation, and inertia estimation. Both simulations and experiments have exhibited superior performance and a promising application perspective of the proposed scheme.

References

[1] Y. Yao, Y. Huang, F. Peng, J. Dong, and Z. Zhu, "Compensation method of position estimation error for high-speed surface-mounted PMSM drives based on robust inductance estimation," *IEEE Trans. Power Electron.*, vol. 37, no. 2, pp. 2033–2044, Feb. 2022.

[2] Y. Bai et al., "High-gain nonlinear active disturbance rejection control strategy for traction permanent magnet motor drives," *IEEE Trans. Power Electron.*, vol. 37, no. 11, pp. 13135–13146, Nov. 2022.

[3] T. Tarczewski, R. Szczepanski, K. Erwinski, X. Hu, and L. M. Grzesiak, "A novel sensitivity analysis to moment of inertia and load variations for PMSM drives," *IEEE Trans Power Electron.,* vol. 37, no. 11, pp. 13299–13309, Nov. 2022.

[4] C. Gong, Y. Hu, K. Ni, J. Liu, and J. Gao, "SM load torque observer-based FCS-MPDSC with single prediction horizon for high dynamics of surface-mounted PMSM," *IEEE Trans. Power Electron.*, vol. 35, no. 1, pp. 20–24, Jan. 2020.

[5] A. K. Junejo, W. Xu, C. Mu, M. M. Ismail, and Y. Liu, "Adaptive speed control of PMSM drive system based a new sliding-mode reaching law," *IEEE Trans. Power Electron.*, vol. 35, no. 11, pp. 12110–12121, Nov. 2020.

[6] V. Q. Leu, H. H. Choi, and J.-W. Jung, "Fuzzy sliding mode speed controller for PM synchronous motors with a load torque observer," *IEEE Trans. Power Electron.*, vol. 27, no. 3, pp. 1530–1539, Mar. 2012.

[7] X. Zhang and Z. Li, "Sliding-mode observer-based mechanical parameter estimation for permanent magnet synchronous motor," *IEEE Trans. Power Electron.*, vol. 31, no. 8, pp. 5732–5745, Aug. 2016.

[8] X. Sun, J. Wu, G. Lei, Y. Guo, and J. Zhu, "Torque ripple reduction of SRM drive using improved direct torque control with sliding mode controller and observer," *IEEE Trans. Ind. Electron.*, vol. 68, no. 10, pp. 9334–9345, Oct. 2021.

[9] X. Zhang, L. Sun, K. Zhao, and L. Sun, "Nonlinear speed control for PMSM system using sliding-mode control and disturbance compensation techniques," *IEEE Trans. Power Electron.*, vol. 28, no. 3, pp. 1358–1365, Mar. 2013.

[10] K. Ohnishi, M. Shibata, and T. Murakami, "Motion control for advanced mechatronics," *IEEE/ASME Trans. Mechatronics*, vol. 1, no. 1, pp. 56–67, Mar. 1996.

[11] S. Li, M. Zhou, and X. Yu, "Design and implementation of terminal sliding mode control method for PMSM speed regulation system," *IEEE Trans. Ind. Inform.*, vol. 9, no. 4, pp. 1879–1891, Nov. 2013.

[12] Y. Wang, Y. Feng, X. Zhang, and J. Liang, "A new reaching law for antidisturbance sliding-mode control of PMSM speed regulation system," *IEEE Trans. Power Electron.*, vol. 35, no. 4, pp. 4117–4126, Apr. 2020.

[13] H. Liu and S. Li, "Speed control for PMSM servo system using predictive functional control and extended state observer," *IEEE Trans. Ind. Electron.*, vol. 59, no. 2, pp. 1171–1183, Feb. 2012.

[14] Z. Chen, A. A. Dawara, X. Zhang, H. Zhang, C. Liu, and G. Luo, "Adaptive sliding mode observer-based sensorless control for SPMSM employing a dual-PLL," *IEEE Trans. Transp. Electrific.*, vol. 8, no. 1, pp. 1267–1277, Mar. 2022.

[15] Y. Zuo, J. Mei, X. Zhang, and C. H. T. Lee, "Simultaneous identification of multiple mechanical parameters in a servo drive system using only one speed," *IEEE Trans. Power Electron.*, vol. 36, no. 1, pp. 716–726, Jan. 2021.

[16] Y. Feng, X. Yu, and F. Han, "High-order terminal sliding-mode observer for parameter estimation of a permanent-magnet synchronous motor," *IEEE Trans. Ind. Electron.*, vol. 60, no. 10, pp. 4272–4280, Oct. 2013.

[17] H.-W. Kim, H.-J. Kim, and J.-Y. Choi, "Multiparameter identification for SPMSMs using NLMS adaptive filters and extended sliding-mode observer," *IET Electr. Power Appl.*, vol. 14, no. 4, pp. 533–543, Apr. 2020.

[18] S. Zhao, Y. Chen, and Y. Mao, "Adaptive load observer-based feed-forward control in PMSM drive system," *Trans. Inst. Meas. Control.*, vol. 37, no. 3, pp. 414–424, Aug. 2015.

[19] F.-J. Lin, "Robust speed-controlled induction-motor drive using EKF and RLS estimators," *IEE Proc.-Electr. Power Appl.*, vol. 143, pp. 186–192, May 1996.

[20] R. Kelly, J. Llamas, and R. Campa, "A measurement procedure for viscous and coulomb friction," *IEEE Trans. Instrum. Meas.*, vol. 49, no. 4, pp. 857–861, Aug. 2000.

[21] C. Yang, B. Song, Y. Xie, S. Lu, and X. Tang, "Speed-controller-independent mechanical parameter identification in SPMSM drive achieved via signal injection," *IEEE Trans. Ind. Electron.*, vol. 70, no. 2, pp. 1282–1297, Feb. 2023.

[22] S. Kim, "Moment of inertia and friction torque coefficient identification in a servo drive system," *IEEE Trans. Ind. Electron.*, vol. 66, no. 1, pp. 60–70, Jan. 2019.

[23] C.-Y. Chen and M.-Y. Cheng, "Adaptive disturbance compensation and load torque estimation for speed control of a servomechanism," *Int. J. Mach. Tools Manuf.*, vol. 59, pp. 6–15, Aug. 2012.

[24] H. S. Lee and M. Tomizuka, "Robust motion controller design for high-accuracy positioning systems," *IEEE Trans. Ind. Electron.*, vol. 43, no. 1, pp. 48–55, Feb. 1996.

[25] J.-C. Wu, K.-H. Su, and M.-Y. Cheng, "Friction and disturbance compensation for speed control of servo control systems," in *Proc. IEEE 36th Annu. Conf. Ind. Electron. Soc.*, 2010, pp. 1890–1895.

[26] L. Chai and F. Yao, "Sliding mode control with friction observer and load observer of PMSM," in *Proc. IEEE 15th Int. Conf. Control, Autom. Syst.*, 2015, pp. 1102–1106.

[27] R. Szczepanski, T. Tarczewski, L. J. Niewiara, and D. Stojic, "Identification of mechanical parameters in servo-drive system," in *Proc. IEEE 19th Int. Power Electron. Motion Control Conf.*, 2021, pp. 566–573.

[28] X. Chen, X. Wei, G. Yang, and W. Du, "Fireworks explosion based artificial bee colony for numerical optimization," *Knowl. Based Syst.*, vol. 188, Jan. 2020, Art. no. 105002.

[29] L. Cui et al., "Modified Gbest-guided artificial bee colony algorithm with new probability model," *Soft Comput.*, vol. 22, pp. 2217–2243, Jan. 2018.

[30] A. Janot, P. C. Young, and M. Gautier, "Identification and control of electro-mechanical systems using state-dependent parameter estimation," *Int. J. Control*, vol. 90, no. 4, pp. 643–660, Jul. 2017.

[31] W. Lu et al., "A new load torque identification sliding mode observer for permanent magnet synchronous machine drive system," *IEEE Trans. Power Electron.*, vol. 34, no. 8, pp. 7852–7862, Aug. 2019.

[32] C. Lian, F. Xiao, S. Gao, and J. Liu, "Load torque and moment of inertia identification for permanent magnet synchronous motor drives based on sliding mode observer," *IEEE Trans. Power Electron.*, vol. 34, no. 6, pp. 5675–5683, Jun. 2019.

[33] K.-B. Lee and F. Blaabjerg, "Robust and stable disturbance observer of servo system for low-speed operation," *IEEE Trans. Ind. Appl.*, vol. 43, no. 3, pp. 627–635, May/Jun. 2007.

[34] S.-J. Hong, H.-W. Kim, and S.-K. Sul, "A novel inertia identification method for speed control of electric machine," in *Proc. IEEE 22nd Int. Conf. Ind. Electron., Control, Instrum.*, 1996, pp. 1234–1239.

[35] S. Wang and S. Wan, "Estimations of load parameters for PMSM by MRAS," in *Proc. IEEE Int. Conf. Elect. Control Eng.*, 2011, pp. 657–660.

[36] J. Linares-Flores, J. Reger, and H. Sira-Ramírez, "Load torque estimation and passivity-based control of a boost-converter/DC-motor combination," *IEEE Trans. Control Syst. Technol.*, vol. 18, no. 6, pp. 1398–1405, Nov. 2010.

[37] C. Yang, B. Song, Y. Xie, and X. Tang, "Online parallel estimation of mechanical parameters for PMSM drives via a network of interconnected extended sliding-mode observers," *IEEE Trans. Power Electron.*, vol. 36, no. 10, pp. 11818–11834, Oct. 2021.

[38] H. Kim, J. Son, and J. Lee, "A high-speed sliding-mode observer for the sensorless speed control of a PMSM," *IEEE Trans. Ind. Electron.*, vol. 58, no. 9, pp. 4069–4077, Sep. 2011.

[39] A. Ammar, A. Bourek, and A. Benakcha, "Nonlinear SVM-DTC for induction motor drive using input-output feedback linearization and high order sliding mode control," *ISA Trans.*, vol. 67, pp. 428–442, 2017.

[40] M. M. Amin, F. F. M. El-Sousy, O. A. Mohammed, G. A. A. Aziz, and K. Gaber, "MRAS-based super-twisting sliding-mode estimator combined with block control and DTC of six-phase induction motor for ship propulsion application," *IEEE Trans. Ind. Appl.*, vol. 57, no. 6, pp. 6646–6658, Nov./Dec. 2021.

[41] B. Wang, C. Luo, Y. Yu, G. Wang, and D. Xu, "Antidisturbance speed control for induction machine drives using high-order fast terminal sliding-mode load torque observer," *IEEE Trans. Power Electron.*, vol. 33, no. 9, pp. 7927–7937, Sep. 2018.

[42] G. Zhang, G. Wang, D. Xu, and N. Zhao, "ADALINE-network-based PLL for position sensorless interior permanent magnet synchronous motor drives," *IEEE Trans. Power Electron.*, vol. 31, no. 2, pp. 1450–1460, Feb. 2016.

[43] T. Liu, Z. Ye, and G. Griepentrog, "Comparison of online inertia identification methods for permanent magnet synchronous motor," in *Proc. IEEE PCIM Europe, Int. Exhib. Conf. Power Electron., Intell. Motion, Renewable Energy Energy Manage.*, 2019, pp. 1890–1893.

[44] C. Yang, B. Song, Y. Xie, S. Lu, and X. Tang, "Stable simultaneous inertia and disturbance torque identification for SPMSM drive systems subject to mismatched rotor flux linkage," *IEEE J. Emerg. Sel. Topics Power Electron.*, vol. 10, no. 2, pp. 2445–2462, Apr. 2022.

[45] S. Kobayashi, I. Awaya, H. Kuromaru, and K. Oshitani, "Dynamic model based auto-tuning digital servo driver," *IEEE Trans. Ind. Electron.*, vol. 42, no. 5, pp. 462–466, Oct. 1995.

[46] L. Niu, D. Xu, M. Yang, X. Gui, and Z. Liu, "On-line inertia identification algorithm for PI parameters optimization in speed loop," *IEEE Trans. Power Electron.*, vol. 30, no. 2, pp. 849–859, Feb. 2015.

[47] J. A. Moreno and M. Osorio, "A Lyapunov approach to second-order sliding mode controllers and observers," in *Proc. IEEE 47th Conf. Decis. Control*, 2008, pp. 2856–2861.

[48] Q.-K. Wang, Y.-J. He, J.-N. Shen, X.-S. Hu, and Z.-F. Ma, "State of charge-dependent polynomial equivalent circuit modeling for electrochemical impedance spectroscopy of lithium-ion batteries," *IEEE Trans. Power Electron.*, vol. 33, no. 10, pp. 8449–8460, Oct. 2018.

[49] S.-H. Lee, J.-S. Yim, J.-H. Lee, and S.-K. Sul, "Design of speed control loop of a variable speed diesel engine generator by electric governor," in *Proc. IEEE Ind. Appl. Soc. Annu. Meeting*, 2008, pp. 1–5.

[50] J. Yang, W.-H. Chen, S. Li, L. Guo, and Y. Yan, "Disturbance/uncertainty estimation and attenuation techniques in PMSM drives—A survey," *IEEE Trans. Ind. Electron.*, vol. 64, no. 4, pp. 3273–3285, Apr. 2017.

[51] L. Niewiara, T. Tarczewski, and L. Grzesiak, "Application of extended Kalman filter for estimation of periodic disturbance and velocity ripple reduction in PMSM drive," *Bull. Polish Acad. Sci. Tech. Sci.*, vol. 68, no. 5, pp. 983–995, Oct. 2020.
[52] L. J. Niewiara, T. Tarczewski, and L. M. Grzesiak, "Application of state feedback controller with feedforward for velocity ripples reduction of PMSM drive at low speed operation," in *Proc. IEEE 21st Eur. Conf. Power Electron. Appl.*, 2019, pp. 1–10.
[53] X. Zhu, H. Zhang, B. Yang, and G. Zhang, "Cloud-based shaft torque estimation for electric vehicle equipped with integrated motor-transmission system," *Mech. Syst. Signal Process.*, vol. 99, pp. 647–660, Jan. 2018.
[54] Y. Wang, L. Gu, Y. Xu, and X. Cao, "Practical tracking control of robot manipulators with continuous fractional-order nonsingular terminal sliding mode," *IEEE Trans. Ind. Electron.*, vol. 63, no. 10, pp. 6194–6204, Oct. 2016.
[55] W.-S. Huang, C.-W. Liu, P.-L. Hsu, and S.-S. Yeh, "Precision control and compensation of servomotors and machine tools via the disturbance observer," *IEEE Trans. Ind. Electron.*, vol. 57, no. 1, pp. 420–429, Jan. 2010.

Chengbo Yang (Student Member, IEEE) received the B.S. degree in mechanical design manufacturing and automation from Southwest University, Chongqing, China, in 2018. He is currently working toward the Ph.D. degree in mechanical engineering with the Huazhong University of Science and Technology, Wuhan, China.

He is an active reviewer of IEEE TRANSACTIONS ON INDUSTRIAL ELECTRONICS and IEEE TRANSACTIONS ON TRANSPORTATION ELECTRIFICATION. His research interests include parameter estimation, servo control, and intelligent technology.

Bao Song received the Ph.D. degree in mechanical engineering from the Huazhong University of Science and Technology (HUST), Wuhan, China, in 2005.

From 2006 to 2008, she performed Postdoctoral Research with The Hong Kong University of Science and Technology, Hong Kong. She is currently a Professor with the School of Mechanical Science and Engineering, HUST. She has authored or coauthored more than 50 academic papers and obtained more than 20 invention patents. Her research interests include servo control, parameter estimation, and field-bus technology.

Yuanlong Xie (Member, IEEE) received the B.S. degree in electrical engineering and the Ph.D. degree in mechanical engineering from the Huazhong University of Science and Technology (HUST), Wuhan, China, in 2014 and 2018, respectively.

From 2017 to 2018, he was an Academic Visitor with the School of Electronic and Electrical Engineering, University of Leeds, Leeds, U.K. Since November 2018, he has been a Postdoctoral Fellow with HUST. He has authored or coauthored more than 60 academic journal and conference papers, one book, and held more than 15 patents. His research interests include robot control, servo control, field-bus technology, and networked control systems.

Dr. Xie was a recipient of the Best Student Paper Award at the 2020 IEEE Region 10 Conference.

Shiqi Zheng (Senior Member, IEEE) received the Ph.D. degree from the Huazhong University of Science and Technology, Wuhan, China, in 2016.

He is currently a Professor with the China University of Geosciences, Wuhan, China. He has been a Visiting Scholar with the University of Adeleide, Adelaide, SA, Australia. His research interest lies on adaptive and robust control for complex systems, such as robotic systems and motion control.

Xiaoqi Tang received the Ph.D. degree in mechanical engineering from the Huazhong University of Science and Technology (HUST), Wuhan, China, in 1998.

From 1996 to 1998, he was an Academic Visitor with the School of Engineering, The Hong Kong University of Science and Technology, Hong Kong. He is currently a Professor with HUST and the Vice Director of the National NC System Engineering Research Center. He has authored or coauthored more than 100 academic papers and gained more than 40 invention patents. His research interests include servo drives, NC technology, industrial robot control, and intelligent machinery manufacturing.